

A. Ozgurluk, M. Akgul, and C. T.-C. Nguyen, "RF channel-select micromechanical disk filters—part I: design," *IEEE Trans. Ultrason., Ferroelect., Freq. Contr.*, vol. 66, no. 1, pp.192-217, Jan. 2019, DOI: [10.1109/TUFFC.2018.2881727](https://doi.org/10.1109/TUFFC.2018.2881727). (26 pages).

RF Channel-Select Micromechanical Disk Filters, Part I: Design

Alper Ozgurluk, *Student Member, IEEE*, Mehmet Akgul, *Member, IEEE*,
 and Clark T.-C. Nguyen, *Fellow, IEEE*

Abstract— This part one of two papers introduces a design flow for micromechanical RF channel-select filters with tiny fractional bandwidths capable of eliminating strong adjacent channel blockers directly after the antenna, hence reducing the dynamic range requirement of subsequent stages in an RF front-end. Much like VLSI transistor circuit design, the mechanical circuit design flow described herein is hierarchical with a design stack built upon vibrating micromechanical disk building blocks capable of Q 's exceeding 10,000 that enable low filter passband loss for tiny fractional bandwidths. Array-composites of half-wavelength coupled identical vibrating disks constitute a second level of hierarchy that reduces the filter termination impedance. A next level of hierarchy couples array-composites with full-wavelength beams to affect fully-balanced differential operation. Finally, identical differential blocks coupled with quarter-wavelength beams generate the desired passband. Part II of this study corroborates the efficacy of this design hierarchy via experimental results that introduce a 39nm-gap capacitive transducer, voltage-controlled frequency tuning, and differential operation towards demonstration of a 0.1% bandwidth, 223.4-MHz channel-select filter with only 2.7dB of in-band insertion loss and 50dB of stopband rejection.

Index Terms—RF channel selection, MEMS resonator, band-pass filter, mechanical circuit design, circuit model, quality factor, insertion loss, differential, coupling, small gap, frequency tuning.

NOMENCLATURE

Q	Resonator quality factor.
Q_f	Filter quality factor.
f_o	Filter center frequency.
B	Filter 3dB bandwidth.
R_x	Single disk motional resistance.
L_x	Single disk motional inductance.
C_x	Single disk motional capacitance.
R_{xA}	Disk array-composite motional resistance.
L_{xA}	Disk array-composite motional inductance.
C_{xA}	Disk array-composite motional capacitance.
C_c	Shunt coupling capacitance.
C_o	I/O electrode overlap capacitance.
C_t	Tuning electrode overlap capacitance.
C_{oA}	I/O disk array-composite overlap capacitance.
C_{tA}	Tuning disk array-composite overlap capacitance.
R_Q	Filter termination resistance.
C_L	Load capacitance.
C_p	Parasitic capacitance.
f_{FOM}	Low pass cut-off frequency.
γ	Coupling coeff. factor required to avoid distortion.
P_{BW}	Percent bandwidth of the filter.
d_o	Electrode-to-resonator gap spacing.
V_P	dc-bias voltage.
V_T	Tuning voltage.

v_i	ac voltage.
f_l	Lower mode resonance frequency.
f_H	Higher mode resonance frequency.
B_{sep}	Freq. separation between lower and higher modes.
q_n	Mod. factor depending on the filter order and type.
IL	Insertion loss.
k_m	Resonator dynamic stiffness.
k_c	Coupler dynamic stiffness.
k_{ij}	Modification factor needed for the coupler.
h	Disk thickness.
R	Disk radius.
N_{tot}	Total number of disks in an array-quadrant.
N_{Io}	Number of I/O disks in an array-quadrant.
N_t	Number of tuning disks in an array-quadrant.
N_b	Number of buffer disks in an array-quadrant.
N_e	Number of electrode-equipped resonators
ϵ_o	Permittivity of vacuum.
θ_{ov}	Angular overlap between the electrode and the disk.
E	Young's modulus.
ρ	Resonator structural material density.
σ	Poisson ratio.
m	Mode number.
χ	Constant that relates the stat. mass to dynamic mass.
M_{tot}	Single disk static mass.
m_m	Single disk dynamic mass.
f_{nom}	Disk nominal resonance frequency.
J_0	Bessel function of the first kind of order zero.
J_1	Bessel function of the first kind of order one.
α	Mode-dependent scaling factor.
K_{mat}	Dimensionless frequency parameter.
Z_o	Characteristic acoustic impedance.
β	Propagation constant.
w_c	Coupling beam width.
l_c	Coupling beam length.
v_p	Acoustic velocity.
λ	Acoustic wavelength at the vibration frequency.
$l_{c,\lambda/2}$	Half-wavelength coupling beam length.
η_e	I/O electrode coupling coefficient.
η_{eA}	I/O disk array-composite coupling coefficient.
η_t	Tuning electrode coupling coefficient.
η_{tA}	Tuning disk array-composite coupling coefficient.
r_x	Single disk equivalent damping.
l_x	Single disk equivalent dynamic mass.
c_x	Single disk inverse dynamic stiffness
r_{xA}	Array core- LCR equivalent damping.
l_{xA}	Array core- LCR equivalent dynamic mass.
c_{xA}	Array core- LCR eq. inverse dynamic stiffness.
η_c	Inverse mechanical coupler turns ratio.
P_{IIP3}	IIP ₃ power level.

A_o	Overlap area between the electrode and the disk.
k_{re}	Effective stiffness of a single disk at the edge.
k_{reA}	Effective stiffness of a disk array-composite.
$k_{c,ij}$	Stiffness of the coupler beam between i^{th} and j^{th} res.
ζ	Odd multiple of the quarter-wavelength.
$w_{c,min}$	Critical width that can be reliably manufactured.
N_{row}	Number of rows in in an array-quadrant.
N_{col}	Number of columns in in an array-quadrant.
R_{bias}	Parasitic dc-bias line resistance.
$R_{\lambda/4}$	Quarter wavelength coupler resistance.
C_{sub}	Pad-to-substrate capacitance.
C_f	Overhead feedthrough capacitance.
$\sigma_{f,Single}$	Single resonator frequency standard deviation.
Δf	Normalized frequency excursion.
ω_{dim}	Purely mechanical radian resonance frequency.
ω_{binom}	Nominal resonance frequency of array-composite i .
ω_{oi}	Radian resonance frequency of the i^{th} differential array-composite including electrical effects.

I. INTRODUCTION

The power consumption of a radio generally goes as the number and strength of the RF signals it must process [1], [2], [3]. In particular, a radio receiver would consume much less power if the signal presented to its electronics contained only the desired signal in a tiny percent bandwidth frequency channel and no interferers. A recent MEMS-based RF channel-selecting super-regenerative receiver demonstrates this [4], even if only for small bit rates. At higher bit rates, however, RF channel-selection is rare. Instead, the typical mix of signals includes unwanted energy outside the desired channel that may be much stronger than the desired signal, by as much as 60dB for LTE [5] and 80dB for GSM [6]. The more unwanted energy present, the higher the dynamic range required of the electronics, hence, the larger the power consumption. Unfortunately, a lack of filters capable of selecting single channel bandwidths at RF forces the front-ends of contemporary receivers to accept unwanted signals, and thus, to operate with sub-optimal efficiency. Indeed, FBAR or SAW filters, while adept at RF *band*-selection, do not possess sufficient quality factor Q to manage practical RF *channel*-selection without undue insertion loss.

It is no surprise, then, that attempts to realize RF filters with percent bandwidths in the range of 0.1% sufficient to remove all interfering signals, leaving only energy in the desired RF channel, are abundant in the literature [7]. Because the bandwidths of such RF channel-selecting filters are so small, and technologies capable of attaining the needed Q 's are generally not widely tunable, much of the research has focused on micro-scale filters that can assemble into banks of weakly tunable filters, *cf.* Fig. 1, to cover a target communication band.

Because it offers tiny size and very high Q , many research approaches to RF channel-selection focus on MEMS technology. These studies employ various resonator technologies using piezoelectric [8], [9], [10], [11], internal dielectric [12], [13], and capacitive-gap [14], [15], [16], [17], [18] actuation. Unfortunately, so far none of the explored approaches truly achieves the needed performance, which demands not only small percent bandwidth, but also low passband insertion loss and high stop-band rejection. Several approaches explored thus far use resonators, e.g., based on piezoelectric materials [8], [9], that lack

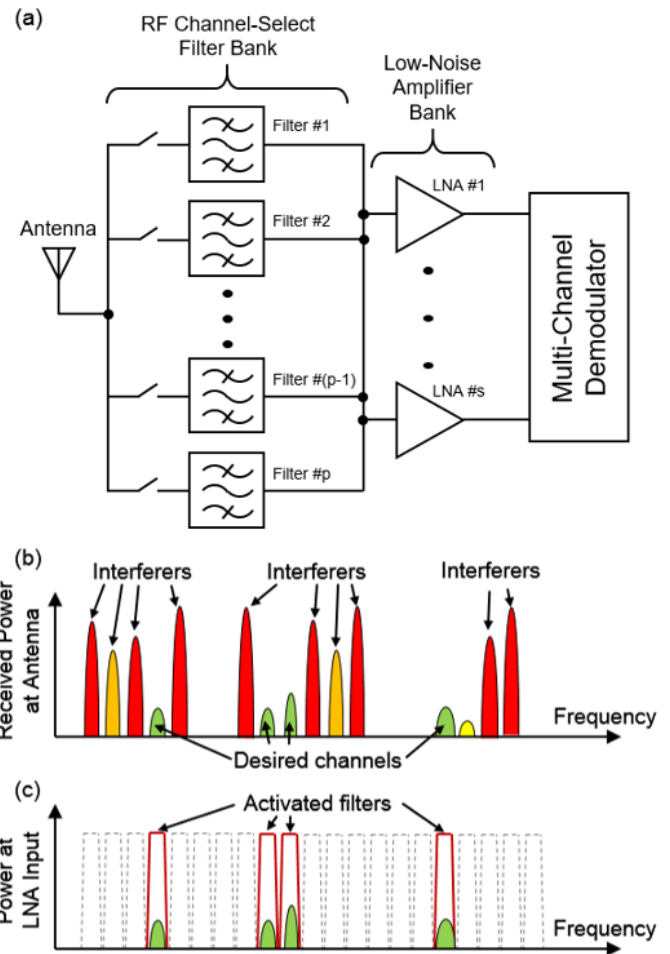


Fig. 1: (a) Direct conversion receiver architecture combined with an RF-channel select filter bank capable of eliminating in-band blockers directly at the RF front-end. (b) Cartoon description of a possible multi-carrier power spectrum that might appear at the antenna of an advanced multi-carrier communication system. (c) On/off configuration of the filters in the RF channelizing filter bank that selects only the desired channels.

the needed Q to achieve low insertion loss in so small a percent bandwidth. For example, one attempt to use conventional attached-electrode piezoelectric resonators does achieve the needed 0.1% bandwidth, but only with excessive passband loss on the order of 15dB [8], which is clearly not permissible immediately after the antenna.

On the other hand, approaches that attain sufficient Q 's on the order of 10,000, e.g., capacitive-gap transduced resonators, so far do not possess enough electromechanical coupling to attain 50dB stop-band rejection at UHF. In particular, although the design of [19] achieves the needed 0.06% bandwidth with an insertion loss of only 2.5dB, it does so with only 27dB of stop-band rejection. It also requires rather large termination impedances on the order of 1.5k Ω that necessitate the use of inductors to resonate out shunt input and output capacitance. Finally, its yield of devices with adequately small passband ripple is quite low.

More recent work using a “capacitive-piezoelectric” transducer that combines capacitive and piezoelectric transduction to realize a resonator with simultaneous high Q and coupling [20] [21] seems poised to eventually achieve RF channel-select filters with appropriate insertion loss and stop-band rejection

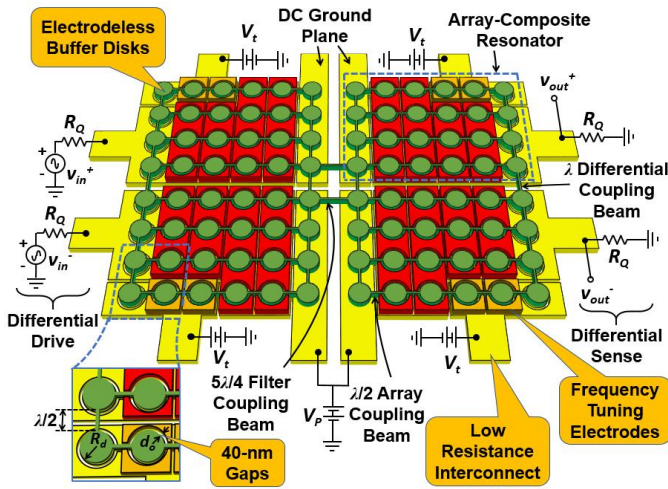


Fig. 2: The improved filter design of this work in a preferred bias and excitation configuration used to evaluate filter performance with indicated improvements over to the filter design of [19] [22].

characteristics. The work of [20], however, demonstrates only a single-resonator that provides only a 2-pole frequency shaping transfer function. Most RF front-ends require at least 4-pole shaping characteristics, i.e., two resonators. Perhaps most importantly, if one transducer technology alone—e.g., one of capacitive-gap or piezoelectric, but not both—can be shown sufficient to achieve the needed filter characteristic, then this would likely be the more cost-effective approach.

This two-part paper focuses on the degree to which capacitive-gap transduced micromechanical resonators can achieve the aforementioned RF channel-selecting filters. It aims in Part I to first show theoretically that with appropriate scaling capacitive-gap transducers are strong enough to meet the needed coupling requirements; and second, to fully detail an architecture and design procedure needed to realize said filters. In Part II, it then provides an actual experimentally demonstrated RF channel-select filter designed using the above procedures and confirming theoretical predictions.

The overall micromechanical circuit design hierarchy used here builds upon micromechanical vibrating disk resonators [23] and uses a combination of capacitive actuation gap scaling [24], coupled array-composites [25], electrical stiffness tuning [26], [27], and fabrication process improvements to attain unprecedented RF channel-select performance [28]. It specifically modifies the design of [19] to that of Fig. 2, which points out the major design changes [22]. Now, smaller electrode-to-resonator gaps on the order of 39nm amplify the input/output electromechanical coupling by more than 8.6 \times , which directly contributes to larger stop-band rejection. The new design also introduces additional electrodes around disks specifically tasked for frequency tuning towards higher circuit yields; as well as carefully designed electrode-less buffer devices that alleviate post-fabrication stress, thereby also contributing to higher yield. Combined, these design changes yield a 223.4-MHz two-resonator filter (described in Part II) that employs 206 resonant micromechanical elements to realize a channel-selecting 0.1%-bandwidth while achieving only 2.7dB of in-band insertion loss together with 50dB of out-of-channel stop-band rejection. This amount of rejection is more than 23dB better than that of [19]

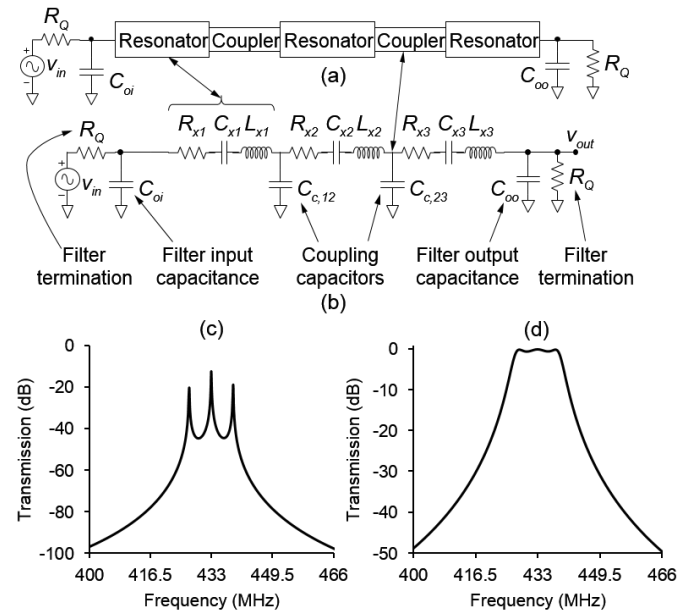


Fig. 3: (a) Schematic description of a popular topology for a resonator-based band-pass filter, comprising a chain of discrete resonator tanks linked with coupling elements. (b) One electrical implementation of (a) using series LCR tanks and shunt capacitor couplers. (c) Underterminated (i.e., $R_Q = 0\Omega$) frequency response of the circuit in (b), showing three distinct peaks denoting the resonance modes of the coupled circuit. (d) Terminated filter response after Q -control via termination resistors R_Q .

and comes in tandem with a 20dB shape factor of 2.7 commensurate with its use of two array-composite resonators.

II. FILTER DESIGN SPECIFICATIONS

Fig. 3 presents the transmission response, i.e., S_{21} with reference impedance R_Q , of a third-order bandpass filter (BPF) and identifies important performance metrics [29], including insertion loss, stopband rejection, passband ripple, group delay ripple, and 20dB shape factor. A common way to achieve filter characteristics as in Fig. 3 is to link multiple two-pole resonators together by coupling elements of some form, as shown in Fig. 3 (a) [29], [30]. Fig. 3 (b) presents one possible implementation that employs series LCR resonator tanks coupled by shunt capacitors to mimic the structure of Fig. 3(a). Here, the resonators realize bandpass biquad transfer functions that when coupled by the shunt capacitors assemble into a frequency response as shown in Fig. 3(c), where three mode peaks ensue, separated by frequency spans governed by coupling strength. Termination of the filter by resistors R_Q then effectively loads the resonators, loading their Q 's and widening their responses so that they add constructively in the passband to form the flat response of Fig. 3(d). Phasing of resonator currents also induces subtraction of their responses outside the passband, thereby providing rejection in the stopband.

The desired filter amplitude response, cf. Fig. 4(a)-(b), minimizes the passband insertion loss, ripple, and the filter 20dB shape factor, the latter defined here by the ratio of the 20dB bandwidth to the 3dB bandwidth; and maximizes the stopband rejection. The group delay characteristic [30] illustrated in Fig. 4(c) is a measure of the degree to which the filter phase response deviates from the ideal linear-phase response. Not only must the group delay be below a certain threshold, its ripple must also be

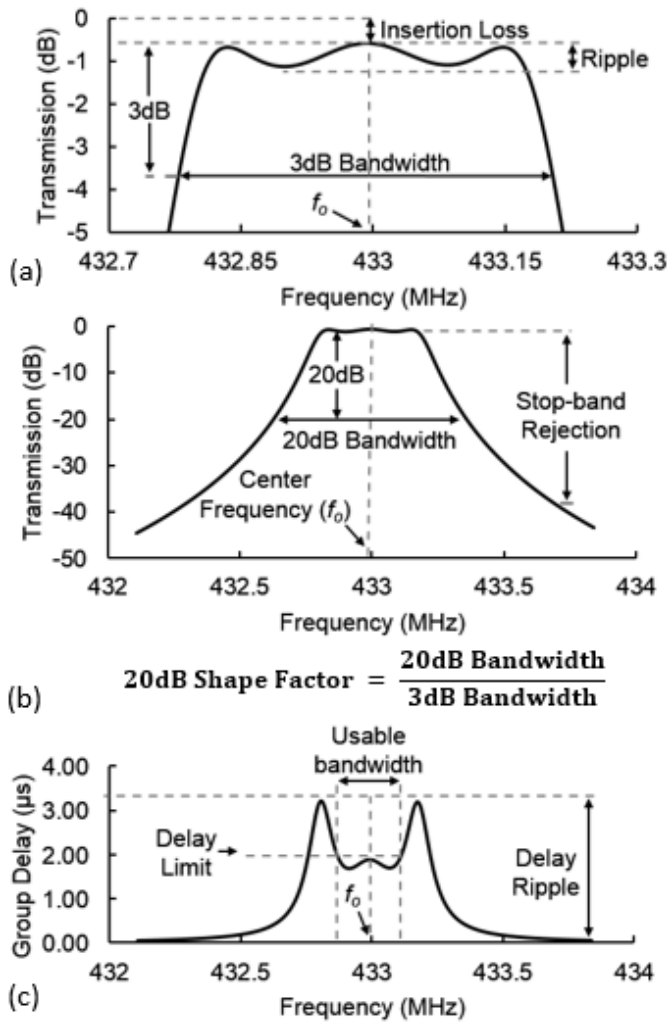


Fig. 4: Graphs defining metrics that gauge bandpass filter performance. (a) Zoom-in on the 3dB passband. (b) Wide-span frequency response. (c) Group delay response.

small. In many cases, the ripple or variation is most important. As a result, in the plot of Fig. 4(c), often only the region of filter bandwidth indicated between the large group delay peaks is actually usable. Note that Chebyshev and Elliptic type filters display a rippled group delay over the passband as seen in Fig. 4, whereas Bessel type filters achieve maximally flat group delay at the expense of increased shape factor [30].

It should be noted that the smaller the percent bandwidth of the filter, the larger the group delay in the usable bandwidth region. Thus, at first glance, it might seem that the 0.1%-bandwidth RF channel-select filters targeted by this work are not usable in a practical application, since they will have larger group delay than the 3%-bandwidth filters typically used in wireless handsets. Such worries, however, are mostly unfounded, since smaller bandwidth signals can withstand larger group delay variations. In other words, slower bit rates can generally tolerate larger delay variations. The important thing is that the bit period-to-group delay variation ratio be above a certain threshold. The smaller the bandwidth of a signal, the larger its bit period, hence the larger the permissible group delay variation.

Group delay is determined primarily by the filter type, i.e., Chebyshev, Butterworth, etc., and bandwidth. Although filter

type also governs passband insertion loss IL and stopband rejection, these very important metrics also depend heavily on the performance of the resonators constituting the filter, particularly their quality factor Q and their input/output transducer coupling, the latter gauged by the (C_x/C_o) ratios of the end resonators in Fig. 3(a). In brief, low filter insertion loss requires sufficient Q ; while proper termination with minimal passband distortion and large stopband rejection requires sufficient electromechanical coupling.

III. NEEDED Q AND COUPLING

Whether or not high resonator Q , strong transducer coupling (C_x/C_o) , or a simultaneous combination of both, are needed, depends largely on the percent bandwidth of the filter to be realized. In particular, the small percent bandwidth filters needed for the aforementioned RF channel-selection application require resonators with large Q to avoid excessive insertion loss, but do not require large (C_x/C_o) .

A. Needed Quality Factor

The insertion loss of a front-end filter is perhaps its most important performance metric. Indeed, the positioning of this filter directly after the antenna and before the low noise amplifier, cf. Fig. 1, means that its loss cannot be attenuated by amplifier gain. As a result, the filter insertion loss ends up adding directly to the receiver noise figure, so often has the greatest impact on overall receiver sensitivity.

The insertion loss of any coupled-resonator filter is primarily determined by the ratio of constituent resonator Q to overall filter quality factor Q_f [29], or

$$q_o = \frac{Q}{Q_f} \quad (1)$$

where Q_f takes the form

$$Q_f = \frac{f_o}{B} \quad (2)$$

where f_o and B are the filter center frequency and 3dB bandwidth, respectively. The filter type and order set the minimum q_o required to achieve a desired insertion loss. Here, filter cookbooks [29] readily provide q_o values for various filter types and insertion losses. For example, the minimum q_o required for less than 2dB insertion loss for a 2nd order Chebyshev filter is 9.7; it increases to 18.6 and 31.1 for third and fourth order filters, respectively [29]. Note that the relation between the quantity set by (1) and the filter insertion loss is independent of the resonator technology used to implement the filter.

Equation (1) implies that the higher the filter Q_f , i.e., the narrower the fractional bandwidth, the higher the constituent resonator Q needed to maintain low insertion loss. Thus, high resonator Q becomes especially important for the small percent bandwidth RF channel-selecting filter targeted, here—much more so than a conventional 3% band-select filter used in today's wireless handsets.

Fig. 5 illustrates the Q dependency by comparing simulated frequency responses of a three-resonator, 0.5dB-ripple, Chebyshev filter operating at 433MHz for band-select and channel-select cases with 3% and 0.1% fractional bandwidths, respectively, with varying constituent resonator Q 's. For these simulations, $C_o = 0$ in order to isolate the effect of Q . Here, large

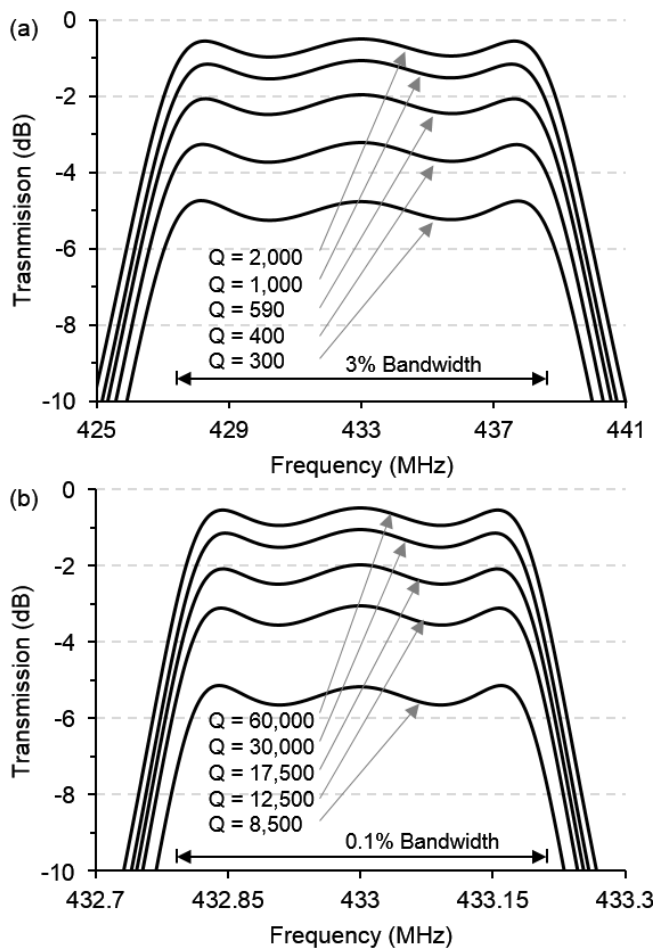


Fig. 5: Simulated frequency characteristics for a 433-MHz three-resonator filter with varying constituent resonator Q 's, illustrating how resonator Q governs the insertion loss of a filter. (b) For an insertion loss less than 2dB, resonator Q 's must be larger than 590 Ω for a 3% bandwidth filter. (c) When the filter bandwidth shrinks to 0.1%, even higher resonator $Q > 17,500$, is needed.

resonator Q clearly minimizes insertion loss, regardless of the percent bandwidth. However, to achieve the same insertion loss, a filter with a smaller percent bandwidth requires resonators with larger Q than one with a large percent bandwidth. For example, the filter with 3% 3dB-bandwidth shown in Fig. 5(a) requires resonator Q 's of 590 to achieve an insertion loss of 2dB. However, when the bandwidth shrinks to the 0.1% required for RF channel-selection (at 433MHz with a 433kHz bandwidth), the required Q for 2dB insertion loss increases to 17,500 as shown in Fig. 5(b). The requirement becomes more stringent as frequencies increase or bandwidths decrease. For example, a 30-kHz bandwidth at 433MHz corresponds to a percent bandwidth of 0.007%, for which the Q required for less than 2dB insertion loss rises to 240,000. The need for Q becomes less stringent as the filter order reduces. For example, a second order version of the 0.1%-bandwidth, 433-MHz filter requires resonator Q 's of only 9,600 to achieve less than 2dB of insertion loss.

B. Needed Electromechanical Coupling Strength

The electromechanical coupling requirement governs proper impedance termination of a given filter. In particular, the flat

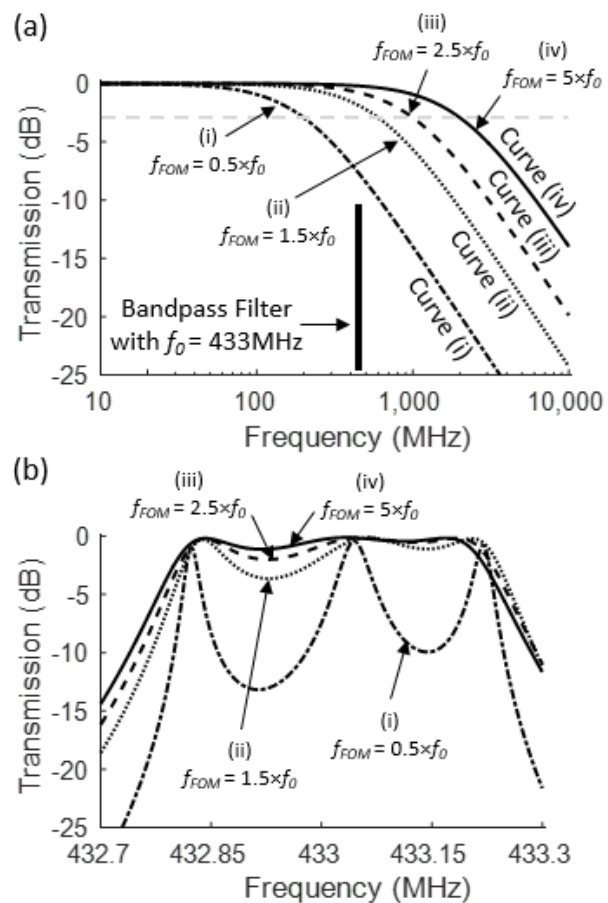


Fig. 6: Simulations illustrating the degree to which low-pass filtering by shunt parasitic capacitance impacts passband flatness for a three-resonator filter, *cf.* Fig. 3, operating at center frequency $f_0 = 433$ MHz. Here, the filter response curves in (b) correspond to the parasitic low-pass filter cases in (a), for which (i) $f_{FOM} = 0.5 f_0$, (ii) $f_{FOM} = 1.5 f_0$, (iii) $f_{FOM} = 2.5 f_0$, and (iv) $f_{FOM} = 5 f_0$.

passbands shown in Fig. 3(d) and Fig. 4(b) are achieved via termination resistors R_Q 's that load the input and output ports, as shown in Fig. 3(a). Here, the R_Q 's essentially load the Q 's of the filter end resonators, smoothing out the passband ripple in the process.

The 50 Ω convention for many discrete parts, e.g., antenna, often stipulates that the R_Q for filters at an RF front-end match to this value. Once past the antenna, however, impedances larger than 50 Ω , in the range of 200-400 Ω , can offer performance enhancements for active circuits. At the intermediate frequency (IF) of super-heterodyne receivers (still used in military applications), impedances in the kilo-ohm range are common. Low power applications also benefit from impedances this high. In summary, the wide variance in application needs calls for a wide range of desirable R_Q 's, and in turn a filter design methodology poised to accommodate.

If the filter had no shunt capacitance C_o at its input and output, then the value of R_Q can be as large or small as needed, with no limit. The presence of C_o , however, places an upper limit on the value of R_Q . In an actual physical realization, load capacitance C_L from leads or other electrically connected structures to the substrate joins C_o to further limit R_Q . In particular, R_Q and $(C_o + C_L)$ combine to form a low pass filter (LPF) that greatly attenuates and distorts the filter response if its cut-off frequency

TABLE I: MINIMUM f_{FOM}/f_o AND C_x/C_o RATIOS THAT ADD LESS THAN 0.5dB RIPPLE TO THE DESIGNED NOMINAL RIPPLE VALUE FOR 0.1% BANDWIDTH FILTERS OF DIFFERENT ORDERS

Filter Type	Filter Order											
	2			3			4			5		
	f_{FOM}/f_o	C_x/C_o	γ	f_{FOM}/f_o	C_x/C_o	γ	f_{FOM}/f_o	C_x/C_o	γ	f_{FOM}/f_o	C_x/C_o	γ
Chebyshev (0.5dB Ripple)	2.36	0.12%	1.2	4.70	0.25%	2.5	5.90	0.32%	3.2	6.75	0.37%	3.7
Chebyshev (0.1dB Ripple)	1.82	0.13%	1.3	3.75	0.26%	2.6	4.47	0.33%	3.3	4.98	0.38%	3.8
Legendre	-	-	-	2.95	0.25%	2.5	4.79	0.44%	4.4	5.54	0.58%	5.8

is below the filter center frequency f_o , such as depicted by curve (i) in Fig. 6(a), which distorts the filter passband as shown in Fig. 6(b). Here, the low pass cut-off frequency is labeled f_{FOM} to emphasize its role as a figure of merit for a given resonator/filter design, where the higher its value, the less passband distortion incurred. Even if f_{FOM} is higher than the filter's center frequency, cf. curve (ii) with simulated response in Fig. 6(b), phase shift from the LPF can still generate significant passband distortion that may or may not be acceptable, depending upon the application. Thus, it is not enough for f_{FOM} to just be higher than f_o . As a rule of thumb, for the case of a three-resonator Chebyshev BPF, the amount of passband distortion introduced by the parasitic LPF is generally acceptable when f_{FOM} is more than 2.5 times the BPF center frequency, as shown by curves (iii) and (iv).

For the case where C_o dominates over C_L , the quantity (C_x/C_o) becomes a very convenient figure of merit for comparison of electromechanically transduced resonators used in a filter. In this case, a rule of thumb to avoid passband distortion upon proper termination stipulates that the transducer coupling at the input and output resonators of a given filter should satisfy

$$\frac{C_x}{C_o} > \gamma P_{BW} \quad (3)$$

where P_{BW} is the percent bandwidth of the filter given as B/f_o ; and γ is 2.5 for a low insertion loss 3-resonator Chebyshev filter, and ~ 6 for a 3-resonator linear phase filter.

Fig. 7 illustrates the dependence of passband distortion on (C_x/C_o) by plotting simulated responses for (a) a 3% bandwidth and (b) a 0.1% bandwidth 3-resonator Chebyshev filter with 0.5dB designed ripple for varying values of transducer (C_x/C_o) . As shown, the passband of the filter in Fig. 7(a) remains relatively undistorted until the transducer (C_x/C_o) drops to below 7.5%, at which point an amount of extra ripple equal to the original 0.5dB ripple appears in the passband for a total of 1dB ripple. On the other hand, the passband ripple of the 0.1% bandwidth filter of Fig. 7(b) worsens to 1dB when (C_x/C_o) drops to a much smaller 0.25%. Note that the passband distortions for both filters conform to the guideline of (3). Table I presents more information on what values of f_{FOM} and (C_x/C_o) maintain ripple to acceptable values.

From Fig. 7, the smaller the percent bandwidth, the smaller the needed (C_x/C_o) . In particular, for a 0.1% bandwidth suitable

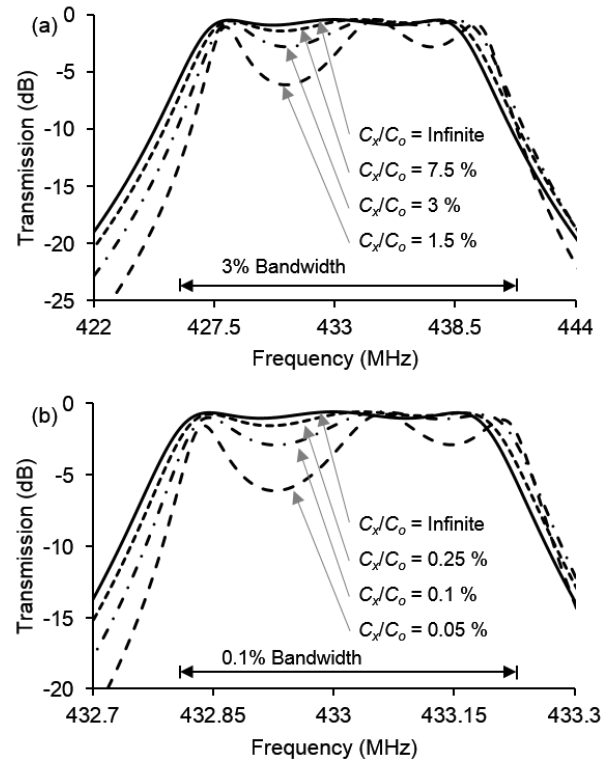


Fig. 7: Simulated plots of responses for (a) a 3% bandwidth and (b) a 0.1% bandwidth 3-resonator Chebyshev filter with 0.5dB designed ripple for varying values of transducer (C_x/C_o) . Here, the simulations use resonator Q 's of 2,500 in (a), and 50,000 in (b).

for RF channel-selection, (C_x/C_o) need only be $\sim 0.25\%$. It is important to note that the needs of a 0.1% RF channel-select filter differ significantly from those of conventional 3% band-select filters used in today's handsets. In particular, conventional 3% filters put a premium on strong coupling, where $(C_x/C_o) \sim 7\%$ is common, and not so much on Q , for which 600 is often acceptable as in Fig. 5(a). On the other hand, a 0.1% RF channel-select filter places a high premium on Q , which must often be greater than 10,000, and not so much on (C_x/C_o) , for which values of only 0.25% are often acceptable.

IV. SIMPLIFIED DESCRIPTION OF VIBRATING DISK FILTER OPERATION

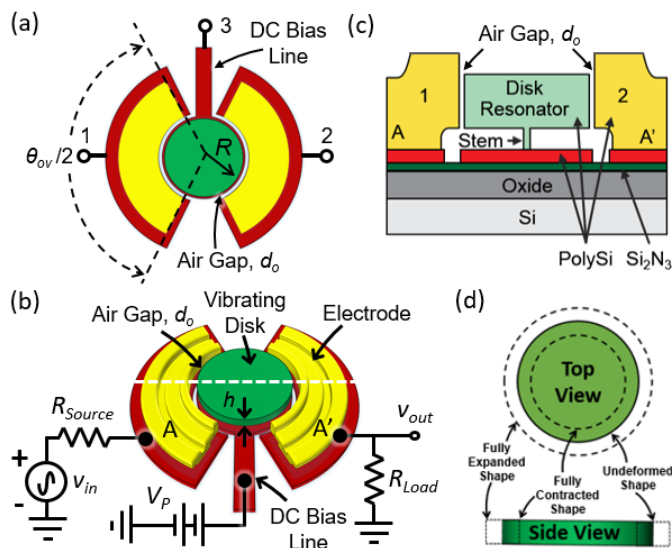


Fig. 8: Pictorial summary for a micromechanical disk resonator with two input/output ports and a resonator body port. (a) Layout view. (b) Perspective view in a typical drive and sense configuration. (c) Cross-section view. (d) Radial-contour vibration mode shape.

The mechanical filter of this work is much like the filter of Fig. 4(b), except that instead of LCR tanks constrained to Q 's below 100, it uses mechanically coupled arrays of vibrating micromechanical resonators [23] capable of achieving Q 's exceeding 10,000. As shown in Fig. 8, each such resonator comprises an electrically conductive disk surrounded by electrodes spaced by small gap spacing d_o from its perimeter, and supported at its center by a stem post, as described in Fig. 8(c).

To operate the disk, a dc-bias voltage V_P is applied to its conductive structure (via terminal 3) and ac voltages $v_i = V_i \cos(2\pi ft)$ are applied at one or both of its electrodes. The combinations of DC and AC voltages applied across each affected electrode-to-resonator gap generate forces on the disk structure at frequency f that then actuate the disk into vibration with amplitude governed by its high Q force-to-velocity bandpass bi-quad transfer function. In particular, when f matches the disk resonance frequency f_o , the disk responds by vibrating with a large (e.g., several nanometers) resonance amplitude in the radial-contour mode shape depicted in Fig. 8(d), where the disk expands and contracts radially around its circumference in a motion reminiscent of breathing. Vibration of the disk gives rise to time-varying capacitors at each electrode-to-resonator interface. Since these capacitors have dc-bias voltages across them, they generate currents given by $i_o = V_P dC/dt$ that can then serve as outputs at selected electrodes.

As shown in Fig. 2 and detailed later in Section VIII, the actual filter uses arrays of many disk resonators that combine currents and add stiffnesses to reduce impedance and tailor bandwidth, respectively. Ignoring the arraying for now (for simplicity), Fig. 9(a) presents a two-disk version of a micromechanical filter for the purposes of explaining its operation. Here, the two disks coupled by a single quarter-wavelength extensional mode beam are identical in all respects, i.e., they have the same resonance frequency. From a mechanical perspective, mechanical coupling of the two resonators creates a two-degree-of-freedom mechanical system that effectively splits the originally identical

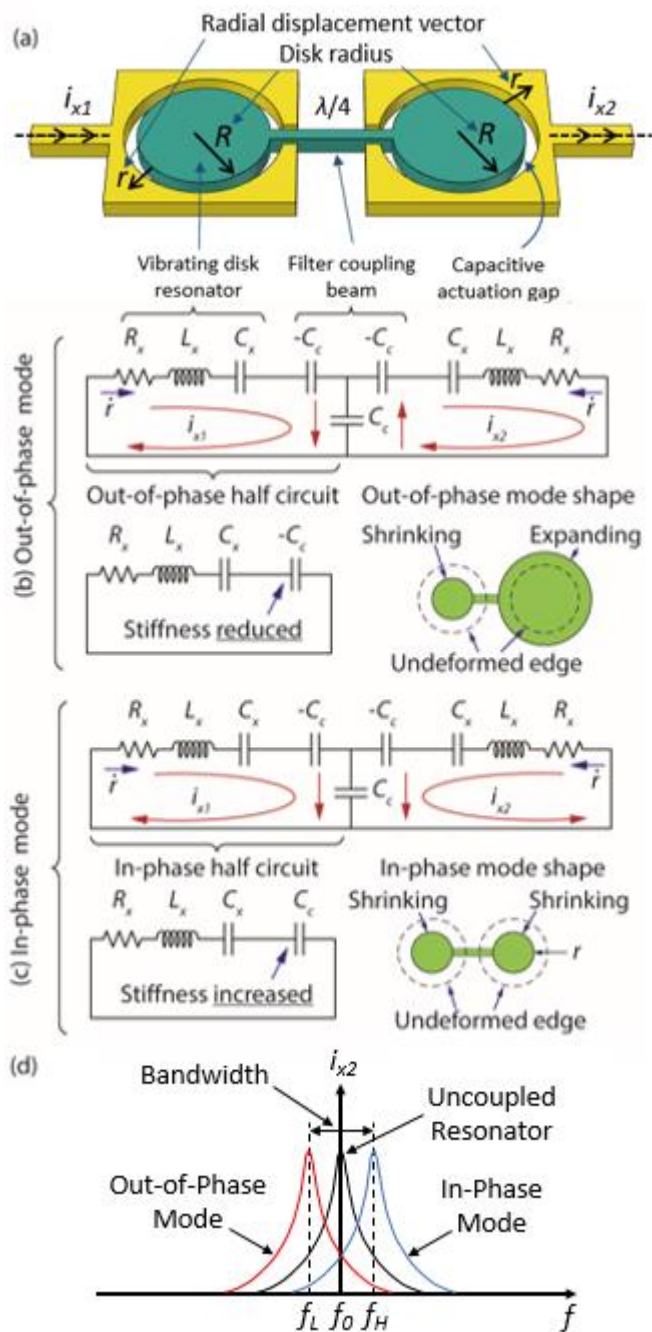


Fig. 9: (a) Schematic description of a mechanically coupled two-disk-resonator filter. Equivalent circuit models for (b) the lower frequency out-of-phase and (c) the higher frequency in-phase filter mode shapes. (d) Motional current spectra for the uncoupled vibrating disk and the lower and higher frequency filter modes.

resonance frequencies of the disks apart into two mode frequencies, i.e., eigenstates, which now define the passband of the filter response. The two modes can be characterized as *out-of-phase*, where the two resonators vibrate with opposite phase, i.e., one expanding while the other contracts at a given instant, cf. Fig. 9(b); and *in-phase*, where the disks expand and contract in unison, cf. Fig. 9(c).

The mechanism by which the quarter-wavelength coupling beam splits frequencies follows from study of the electrical equivalent circuit for this system, shown in Fig. 9 [14]. Here,

LCR tanks model each disk resonator, while a *T*-network of capacitors models the quarter-wavelength coupling beam, essentially treating it as an acoustic transmission line. As shown in [14] [15], the values of the L_x , C_x , and R_x elements in the *LCR*'s are derived directly from the values of mass, stiffness, and damping of the actual resonators.

In the lower frequency *out-of-phase* mode described in Fig. 9(b), the coupling spring experiences no strain, since the adjacent disk edges displace in opposite radial directions. In this mode, the coupling spring contributes no stiffness, only mass, to the total system, which lowers the frequency relative to the original resonators. This means the current into the leftmost (input) disk at resonance, given by

$$i_{x1} = \frac{v_i}{R_x} \quad (4)$$

is positive; and the current going into the rightmost (output) disk is negative, i.e., current flows out of the disk into the output electrode. Thus, current flows through the device, from input to output. This means the motional currents indicated as i_{x1} and i_{x2} in the electrical equivalent circuit flow in the same clockwise directions around their respective meshes. They thus cancel in the shunt capacitor C_c , which means the voltage drop across the shunt arm of the coupling beam *T*-network equals zero. This then yields the half circuit for the system shown in (b), where a capacitor of value $-C_c$ adds in series to the motional C_x of the mechanical resonator, lowering the mesh frequency from that of the original resonator down to the lower mode frequency f_L given by

$$f_L = \frac{1}{2\pi} \sqrt{\frac{1}{L_x} \left(\frac{1}{C_x} - \frac{1}{C_c} \right)} \quad (5)$$

In the higher frequency *in-phase* mode, where both disks vibrate in unison, the coupling spring now experiences strain. This adds stiffness to the system, raising its frequency over that of the original resonators. From the electrical equivalent circuit perspective, the motional currents i_{x1} and i_{x2} in each resonator tank now flow in opposite directions around their respective meshes, which means they add in the shunt C_c arm of the *T*-network. Each mesh thus absorbs half of the shunt C_c to yield the overall half circuit shown in Fig. 9(c), where now a positive C_c adds in series to the motional capacitance C_x . This raises the mesh frequency to

$$f_H = \frac{1}{2\pi} \sqrt{\frac{1}{L_x} \left(\frac{1}{C_x} + \frac{1}{C_c} \right)} \quad (6)$$

Fig. 9(d) plots the motional current amplitude spectrum for an uncoupled individual constituent disk resonating at frequency f_o alongside the coupled out-of- and in-phase mode frequencies at $f_o - B_{sep}/2$ and $f_o + B_{sep}/2$, respectively, where $B_{sep} = f_H - f_L$ is the frequency span that separates the modes. The out-of-phase and in-phase resonance transfer functions illustrated in Fig. 9(d) correspond to the orthogonal eigenvectors of the coupled two-resonator system shown in Fig. 9(a).

The sum of these transfer functions generates the overall filter transfer function, as illustrated in Fig. 10(c). Note that the relative phase between these modes plays a crucial role in shaping the overall filter response. In particular, the out-of-phase and in-phase modes have the same phase between the mode

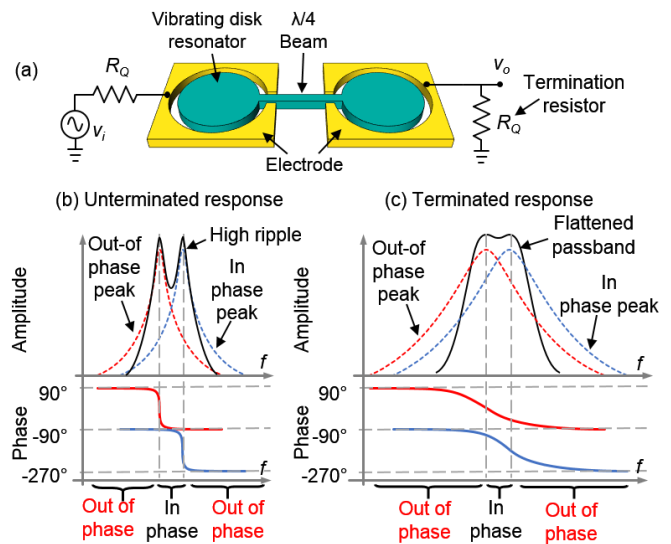


Fig. 10: (a) Mechanically coupled two-resonator filter with termination resistors R_Q added for Q -control. (b) Illustration showing addition of in-phase and out-of-phase resonator frequency responses to create the unterminated filter response. (c) Illustration showing the mechanism for filter response formation after Q -control with appropriate termination resistors R_Q . Note that the plots are not to scale, as the unterminated response would normally be several dB below the terminated response, as depicted in Fig. 3 and described in [14].

peaks, so add constructively within the filter passband to form a flatter response in this region. Outside the peaks, their phases differ by 180° , which means they subtract outside the passband, yielding a steeper roll-off to the stopband and a higher overall stopband rejection.

However, as shown in Fig. 10(b), addition in the passband will not yield a flat passband if the Q 's of the constituent resonators are too high. Indeed, to permit a flat passband, the signal power of each mode spectrum at the frequency directly between the peaks must be approximately equal to half that at the peaks themselves. This is where the termination impedances shown in Fig. 4 and again in Fig. 10(a) become important. These termination resistors R_Q load the Q 's of the resonators, broadening their peaks and effectively raising their power levels at frequencies away from resonance. To attain half power between the peaks, the resonator Q 's must be reduced to approximately that of the filter, or

$$q_n Q_f = Q \left(\frac{R_x}{R_x + R_Q} \right) \rightarrow R_Q = R_x \left(\frac{Q}{q_n Q_f} - 1 \right) \quad (7)$$

where q_n is a modification factor that depends upon the filter order and type, i.e. Chebyshev, Butterworth, and that can be found in filter cookbooks [29]. Upon inclusion of termination resistors R_Q , the flattened passband response in Fig. 10(c) ensues.

From (7), note that for a properly designed filter, R_Q tracks R_x . In other words, a filter designed for a large R_Q uses resonators with large R_x ; and if designed for a small R_Q , the resonators have small R_x . Because of this, the insertion loss of a properly designed filter using (7) is ultimately independent of R_Q . To elaborate using equations, the insertion loss for this two-resonator filter takes the form

$$IL = \frac{R_Q + R_x}{R_Q} = \frac{Q}{Q - q_n Q_f} \quad (8)$$

where tracking of R_Q and R_x effectively cancels them, leaving a rightmost expression that depends only on Q parameters. Thus, insertion loss depends primarily on the resonator Q and the filter Q_f .

From Fig. 10(c), it is clear that with quarter-wavelength coupling the center frequency of the Fig. 10 filter equals the (common) frequency of its constituent resonators; and its 3dB bandwidth is a bit more than the total separation B_{sep} afforded by the coupler strength, captured by the value of C_c . Using (5) and (6), the mode peak separation takes the form

$$B_{sep} = \frac{C_x}{C_c} f_o = \frac{k_c}{k_m} f_o \quad (9)$$

where the last form recognizes that C_x and C_c are proportional to the inverse dynamic stiffnesses k_m and k_c of the resonators and coupler, respectively [14]. Since filter bandwidth is generally the 3dB bandwidth, a modification factor k_{ij} applied to (9) yields the more common form

$$B = \frac{k_c}{k_m k_{ij}} f_o \quad (10)$$

where B is the 3dB bandwidth, and k_{ij} refers to the modification factor needed for the coupler between the i^{th} and j^{th} resonators in a multi-resonator filter. k_{ij} values are widely tabulated in filter cookbooks [29] for a variety of filter types and orders.

It is worth mentioning here that for this electrically driven and sensed filter the R_Q 's serve as source and load impedances. While the R_Q 's do effectively load the Q 's of the resonators, the resonators themselves must have high Q to start with in order to have motional resistances R_x 's sufficiently smaller than R_Q to preserve low insertion loss. In other words, one cannot start with low Q resonators and expect low insertion loss; the resonator Q 's must be high to start with.

V. ACTUAL FILTER STRUCTURE AND OPERATION

Although the actual filter demonstrated in Part II essentially operates as described in the previous section, its overall structure is substantially more complicated, all in the interest of maximizing performance. Again, Fig. 2 presents the perspective-view schematic of the entire mechanical filter circuit in a preferred differential input/output configuration, showing all applied voltages and termination impedances, and pointing out key differences with the previous one of [19] that allow the present design to achieve much improved performance. As shown, the filter comprises 96 disks mechanically coupled by 110 beams. Many of the disks are surrounded by electrodes spaced only 39nm from their edge sidewalls to serve as either input/output or mechanisms for frequency tuning. Array composite resonators are clearly discernable, and their use represents a second level of hierarchy in an overall hierarchical design reminiscent of those used in complex VLSI transistor circuits, but here used to achieve a complex MSI mechanical filter circuit. Fig. 11 illustrates the four main levels of hierarchy that include:

1st Level: Radial-Contour Mode Disk Resonator

The polysilicon contour mode disk resonator depicted in Fig. 8 and described in Section VII comprises the unit element and 1st level of hierarchy in the mechanical circuit. In Fig. 2, all disks are $h=3\mu\text{m}$ -thick with $R=12.1\mu\text{m}$ radii, so share a com-

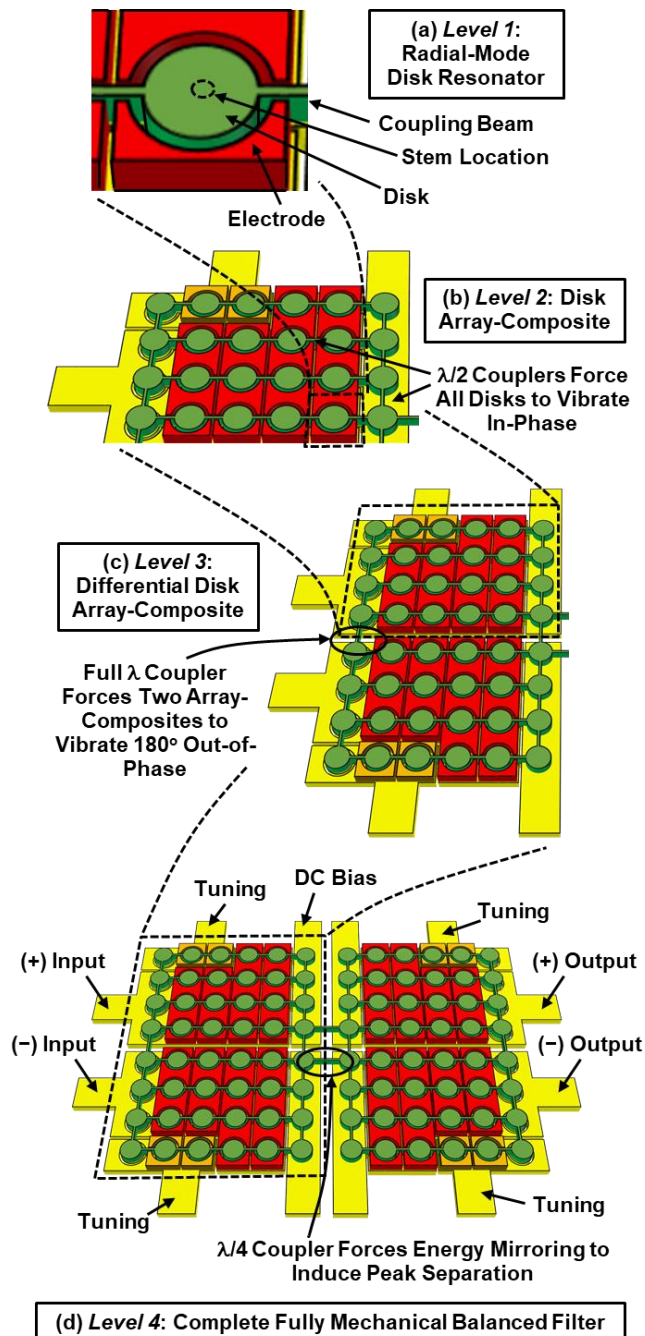


Fig. 11: Pictorial breakdown of the four levels of hierarchy in the disk-array micromechanical filter design. (a) Level 1: Radial-mode capacitive-gap transduced disk resonator. (b) Level 2: Half-wavelength beam-coupled array-composite of disks making up an “array quadrant”. (c) Level 3: Full-wavelength beam-coupled pair of quadrant array-composites for which coupling forces the array-composites to vibrate 180° out-of-phase. (d) Quarter-wavelength beam-coupled differential array-composites that finally make up the total filter.

mon radial-contour mode resonance frequency that sets the center frequency of the overall filter.

2nd Level: Disk Array-Composite

To reduce termination impedance and raise stiffness to facilitate small bandwidth, four array-composites of half-wavelength coupled disks make up the 2nd level of hierarchy. Each combines and raises currents, thereby reducing motional resistance, hence, filter termination impedance.

3rd Level: Differential Array-Composite

To enable differential I/O, a 3rd level of hierarchy couples pairs of array-composites via full-wavelength beams. This forces them to vibrate 180° out-of-phase, thereby enabling differential mode balanced operation that cancels feedthrough to enable large stopband rejection.

4th Level: Coupled Resonator Filter

A 4th level of hierarchy couples the differential blocks via quarter-wavelength beams that split their resonances, generating the desired passband and promoting signal subtraction in the stopband that increases rejection.

Operation of the filter requires the application of a DC voltage V_P to the conductive suspended structure to amplify forces and electrical outputs; and differential electrical inputs through termination impedances (governed by design) to the left-hand terminals. These electrical signals convert to mechanical (e.g., velocity) signals that process mechanically through the frequency response of the structure and then convert back to electrical signals at the outputs.

VI. DETAILED FILTER DESIGN

Given the design hierarchy from the previous section, a sensible design procedure now emerges:

- 1) Design the fundamental micromechanical radial-contour mode disk building block to resonate at the filter center frequency f_o with the needed Q and coupling strength (C_x/C_o) with given values of dc-bias V_P and electrode-to-resonator gap spacing d_o .
- 2) Assemble disks into array-composites to achieve a specific termination resistance R_O , linearity spec, and bandwidth. Here, the array size N_{tot} is key to maintaining practically realizable filter coupling beam dimensions for the chosen filter bandwidth B .
- 3) Design quarter-wavelength filter coupling beams that yield the desired filter passband.
- 4) Convert the design from single-ended to differential.
- 5) Simulate the filter electrical equivalent circuit and verify satisfactory operation in the electrical domain.

Table II and Table III capture this design procedure and provide a preview of the relevant governing equations.

The remainder of this part now expands on the detailed steps and formulations needed to execute each stage of the design process.

VII. RADIAL-CONTOUR MODE DISK DESIGN

The radial-contour mode disk used in this work offers an excellent combination of high Q , reasonable electromechanical coupling (when small gaps are used), and perhaps equally important, mechanical circuit design flexibility. The last of these derives from the fact that a lateral mode disk like that summarized in Fig. 8 is isotropic around its circumference, i.e., it ideally presents the same loading or response at any point on its outside edges. This means that radial beams can attach and couple to a given disk at any angle and still elicit the same response. Such coupling flexibility is quite welcome when complex coupling geometries are required, like the arrays of Fig. 2.

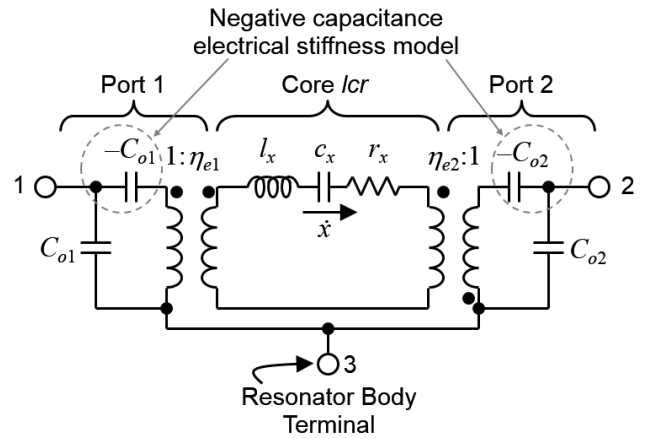


Fig. 12: Negative capacitance small-signal AC equivalent circuit for a two-port capacitive gap transduced micromechanical resonator, such as that of Fig. 8, when operating in the radial-contour mode

The literature is abundant with capacitive-gap-transduced radial-contour mode disk resonators capable of Q 's greater than 29,300 at 153.9MHz in polysilicon structural material [31], and greater than 55,000 at 497.6MHz in polydiamond [32]. Thus, from the perspective of achievable frequency and Q , the chosen disk resonator design seems adequate for RF channel-selection, at least for the example shown in Fig. 5.

From the perspective of electromechanical transducer coupling strength, however, the disk resonators so far reported in the literature have been lacking. For example, the 153.9-MHz polysilicon disk of [31] posted a (C_x/C_o) of only 0.00048%, while a higher frequency 497.6-MHz diamond one was even poorer, on the order of only 0.00005% [32]. Section III.B mentioned that (C_x/C_o) need not be large for RF channel-selection, but these values are abysmal. If disk resonators are to be useful, their design must allow several orders of magnitude improvement in these numbers.

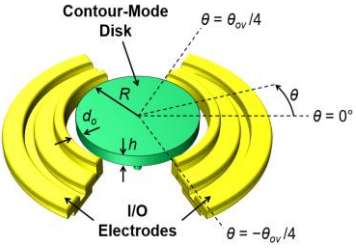
Fortunately, the literature provides comprehensive and experimentally confirmed models for radial-contour mode disk resonators that allow accurate prediction of design-driven performance improvements. Fig. 12 and Table II summarize the equivalent circuit and expressions for elements from [33], respectively, which details the most recent radial-contour mode disk model using a negative capacitance concept. Using formulations from [33], the electromechanical coupling factor for a radial-contour mode disk takes the form

$$\frac{C_x}{C_o} = \frac{V_P^2}{d_o^3} \frac{\epsilon_o R \theta_{ov}}{\pi^3 \chi K_{mat}^2 E} \quad (11)$$

where V_P is the dc-bias applied between the disk resonator and the surrounding electrodes, d_o is the electrode-to-resonator gap spacing, ϵ_o is the permittivity of vacuum, R is the disk radius, θ_{ov} is the angular overlap between the electrode and the disk in radians, and E is the Young's modulus of the resonator structural material. Fig. 8 schematically illustrates these design variables. χ is a constant that relates the static mass M_{tot} of the disk to its dynamic mass m_m as

$$m_m = \chi M_{tot} = \chi \rho \pi R^2 h \quad (12)$$

TABLE II: RADIAL-CONTOUR MODE DESIGN EQUATIONS AND PROCEDURE SUMMARY

Objective/Procedure	Parameter	Relevant Design Equations for a Given Parameter	Eq.
	Resonance Frequency	$f_{nom} = \frac{K_{(R,m),mat}}{2R} \sqrt{\frac{E}{\rho}}$ where $K_{(R,m),mat} = \frac{\zeta_{(R,m),mat}}{\pi\sqrt{2(1+\sigma)}}$ where R denotes the disk radius, E and σ are the Young's modulus and Poisson ratio, and $m =$ mode number.	(13)
	Solve For ζ	$\frac{\zeta J_0(\zeta/\xi)}{\xi J_1(\zeta/\xi)} = 1 - \sigma, \quad \zeta = 2\pi f_{nom} R \sqrt{\frac{2\rho(1+\sigma)}{E}},$ $\xi = \sqrt{\frac{2}{1-\sigma}}$	(14)
<p><u>Given:</u> f_{nom}, V_P, R_x <u>Find:</u> radius R, electrode-to-resonator gap spacing d_o</p> <ol style="list-style-type: none"> Choose E, ρ, and σ by choice of structural material. Choose thickness h. Use (13) to find the R needed to achieve f_{nom}. Use (14) to get ζ in the process. Use (15) to find the d_o needed to achieve R_x. (16)-(18) yield all needed values in the transformer-based negative C_o equivalent circuit. 	Motional Resistance, Capacitance, and Inductance	$R_x = \frac{r_x}{\eta_e^2}, \quad C_x = c_x \eta_e^2, \quad L_x = \frac{l_x}{\eta_e^2}$	(15)
	Core Equiv. Circuit Elements	$l_x = m_m(R) = \frac{2\pi\rho h \int_0^R r J_1^2(\phi r) dr}{J_1^2(\phi R)}, \quad \phi = \omega_o \sqrt{\frac{\rho}{E}(1-\sigma^2)}$ $c_x = \frac{1}{k_m(R)} = \frac{1}{\omega_{nom}^2 m_m}, \quad r_x = b_m(R) = \frac{\sqrt{k_m m_m}}{Q} = \frac{\omega_{nom} m_m}{Q}$	(16)
	Static Overlap Capacitor	$C_o = \frac{\epsilon_o \theta_{ov} R h}{d_o}$	(17)
	Electromechanical Coupling Coeff.	$\eta_e = V_P \frac{C_o}{d_o}$	(18)

where ρ is the resonator structural material density. χ can be derived by consideration of the total kinetic energy of the resonant disk structure and its radial velocity at the disk edges and equals $\chi=0.763, 0.967, 0.987$ for a disk operating in its first, second, and third radial-contour modes, respectively [33].

Since (11) depends on disk radius R , it is a function of disk resonance frequency f_{nom} that derives from the simultaneous solution of [33]

$$\frac{\zeta J_0(\zeta/\xi)}{\xi J_1(\zeta/\xi)} = 1 - \sigma, \quad \xi = \sqrt{\frac{2}{1-\sigma}} \quad (19)$$

and

$$\zeta = 2\pi f_{nom} R \sqrt{\frac{\rho(2+2\sigma)}{E}} \quad (20)$$

where σ is the Poisson ratio of the structural material, and J_0 and J_1 are Bessel functions of the first kind of order zero and one, respectively. Although the solution of (19)-(20) as described provides an accurate value for the contour-mode resonance frequency, it does not readily impart design insight. To provide better insight to variable dependencies, rearrangement and simplification of (19)-(20) yields the closed form

$$f_{nom} = \frac{\alpha K_{mat}}{2R} \sqrt{\frac{E}{\rho}} \quad (21)$$

where α is a mode-dependent scaling factor that accounts for higher order modes, i.e., 1, 2.64, and 4.61 for the 1st, 2nd, and 3rd

radial-contour mode, respectively, and K_{mat} is a dimensionless frequency parameter that depends upon the structural material and is independent of radius [33]. For polysilicon $K_{mat}=0.654$. Solving for R and then inserting into (11) yields the expression for electromechanical coupling as a function of resonance frequency

$$\frac{C_x}{C_o} = \frac{V_P^2}{d_o^3} \frac{\alpha}{f_{nom}} \frac{\epsilon_o \theta_{ov}}{2\pi^3 \chi K_{mat} \sqrt{E\rho}} \quad (22)$$

From (22), a reduction in electrode-to-resonator gap spacing d_o is clearly the most effective approach to raising (C_x/C_o) , given the third power dependence. In fact, reducing d_o from the 80nm used for the 163-MHz disk of [19] to 40nm would increase (C_x/C_o) from 0.022% to 0.177% for a 14V dc-bias voltage—an 8 \times increase that makes possible a 0.177%-bandwidth two-resonator filter at this frequency. At higher frequency, the dependence on radius shown in (11) reduces the efficacy of gap scaling. In particular, for the fundamental mode 1.156-GHz disk of [23] the same 40nm gap and 14V yield a (C_x/C_o) of only 0.024%. An even smaller gap remedies this, where use of the fundamental mode together with 20.6nm and 14V recapture the (C_x/C_o) of 0.177%. This gap sounds small and was indeed once considered impractical, but no longer in light of recent 13-nm gap polysilicon wine-glass disk resonators, which at 60-MHz with 5.5V dc-bias posted a (C_x/C_o) of 1.62% with a Q of 29,640 [34]. Gaps like this should extend the frequency range of disk-array filters well beyond the 223.4 MHz of the Part II paper.

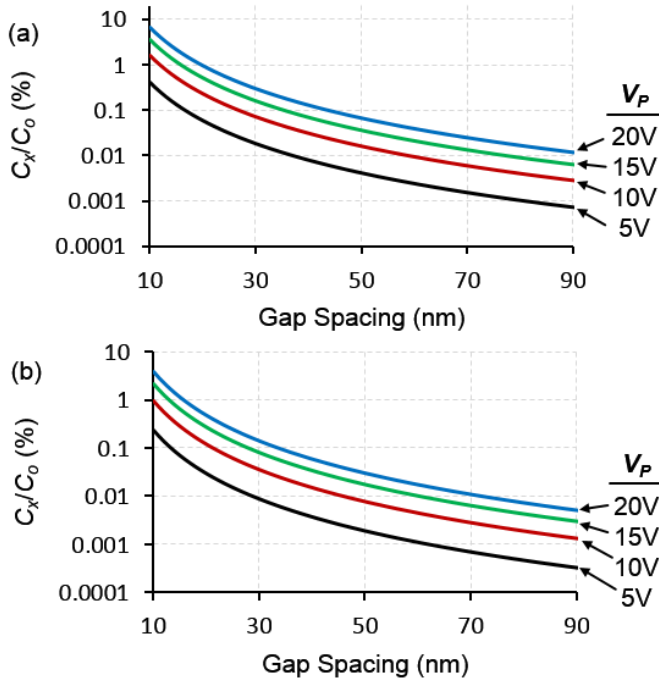


Fig. 13: Simulated plot of C_x/C_0 for a polysilicon contour mode disk resonator with fully surrounding electrodes plotted as a function of the electrode-to-resonator gap spacing for four different bias voltages operating at (a) 433MHz, and (b) 1.2GHz.

Fig. 13 plots (C_x/C_0) versus gap spacings below 100nm for radial-contour mode disks at various frequencies and dc-bias voltages. The chosen V_P voltages are all well below the pull-in voltage for the devices determined both via the classic electrical stiffness pull-in expression and by FEM simulation. Still, other factors might also limit the permissible V_P , e.g., weak stem anchor or electrical breakdown, so the higher voltage plots of Fig. 13 do require validation. Assuming for now that they hold, the plots predict that capacitive-gap transducers with gaps approaching 10nm have potential to achieve (C_x/C_0) \sim 10% at usable RF frequencies. Electromechanical coupling this high is actually not unheard of for capacitive-gap transducers. For example, the clamped-clamped beam resonators used in the HF filter of [15] posted (C_x/C_0)'s on the order of 14.8% at $V_P=35V$.

It should be mentioned that adequate (C_x/C_0) does not guarantee an impedance match with the stages before and after the eventual filter using a given disk resonator. Unfortunately, the tiny size of a single disk relegates it to high impedance. Taking the example of a two-resonator 0.5dB-ripple Chebyshev filter with $q_n=1.9497$ [29] and $Q/Q_f=9.5$ for less than 2dB insertion loss, (7) predicts that a match to a 50Ω R_Q termination requires a motional resistance R_x of 12.9Ω ; and a match to 200Ω requires that R_x be 51.6Ω . Using (15) in Table II with an aggressive (but plausible) gap of $d_o = 20\text{nm}$, the 163-MHz disk reported in [19] with $Q = 10,500$, $h = 3\mu\text{m}$, and $V_P = 14V$, has a (C_x/C_0) of 1.3% (much larger than the 0.06% needed by the filter of [19]) and an R_x of 48Ω . So with the 20-nm gap, the motional resistance of the 163-MHz case is sufficient to permit a filter with 200Ω terminations. It, however, is larger than the needed 12.9Ω for a 50Ω termination even though its (C_x/C_0) is more than sufficient.

The solution: Arraying to further lower R_x without affecting

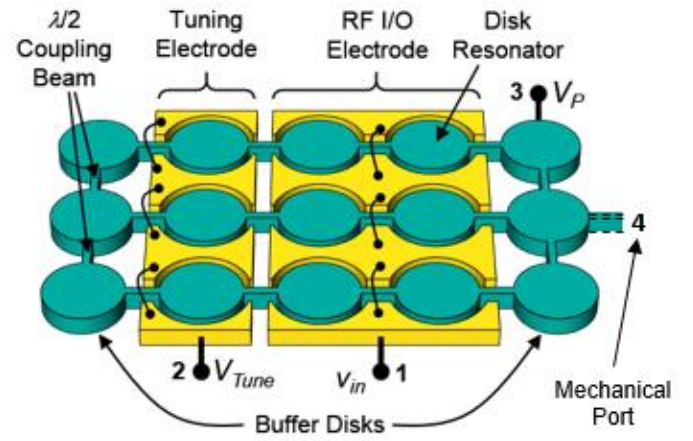


Fig. 14: Illustration of a $\lambda/2$ coupled array-composite resonator with dedicated tuning electrodes and outer buffer disk-resonators for defensive design against in-plane structural film stress.

(C_x/C_0).

VIII. DISK ARRAY-COMPOSITE DESIGN

Section V and Fig. 2 briefly introduced the strategy of arraying N_{io} disk resonators to attain a combined output current N_{io} times larger than that of a single resonator for the same input voltage, i.e., a motional resistance N_{io} times smaller. Of course, the currents of the devices in an array sum constructively only if all devices vibrate in phase and at the same frequency. To insure this, as depicted in Fig. 14, the disks in the array are mechanically strong-coupled by half-wavelength beams that effectively transform the array into a single multi-resonator composite device in which all constituent disks vibrate in unison at one mode frequency. Here, the use of half-wavelength coupling links ideally selects one desired mode and rejects other modes [35]. Its strong coupling also avoids motional resistance reductions predicted for weakly coupled resonator arrays [36]. The result: An array-composite resonator with substantially lower impedance and greater power handling than a single one of its constituents.

The action of the half-wavelength extensional-mode coupling beams is perhaps best understood by closer inspection of the beam itself, depicted in Fig. 16, and its defining chain matrix, which relates the force F and the velocity \dot{x} on both ends of the beam (cf. Fig. 16(a)), taking the form

$$\begin{bmatrix} F_1 \\ \dot{x}_1 \end{bmatrix} = \begin{bmatrix} \cos(\beta l_c) & jY_o \sin(\beta l_c) \\ jZ_o \sin(\beta l_c) & \cos(\beta l_c) \end{bmatrix} \begin{bmatrix} F_2 \\ \dot{x}_2 \end{bmatrix} \quad (23)$$

where Z_o and β , are the characteristic acoustic impedance and propagation constant, respectively, defined in terms of beam thickness h , beam width w_c , beam length l_c , and material properties E and ρ as

$$Y_o = \frac{1}{Z_o} = hw_c \sqrt{\rho E}, \quad \beta = \frac{\omega}{v_p}, \quad v_p = \sqrt{\frac{E}{\rho}} \quad (24)$$

where v_p is the acoustic velocity.

Considering the beam as a mechanical transmission line with acoustic wavelength λ at the desired vibration mode frequency defined as

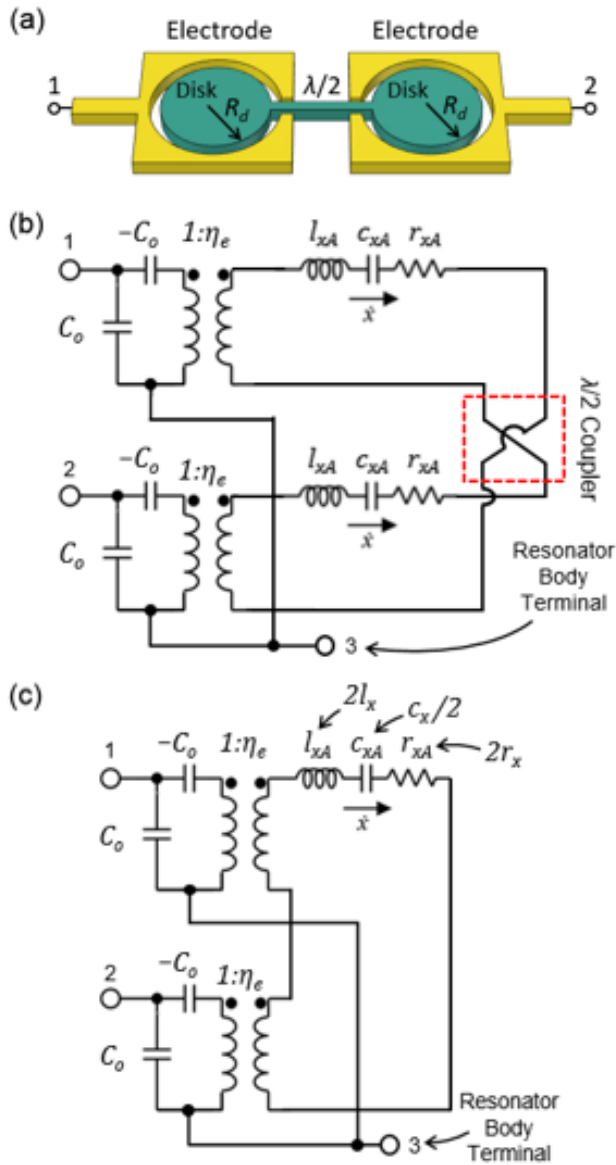


Fig. 17: (a) Schematic view a two-resonator network coupled with a half-wavelength beam. (b) Electrical equivalent circuit representation of the two-resonator array-composite that combines the circuits presented in Fig. 12 and Fig. 16(c); and (c) the same circuit after combining series elements.

two-disk array-composite of Fig. 17(a) results via simple combination of the electrical equivalent circuit representations of the $\lambda/2$ beam presented in Fig. 16(c) and the circuit model of a single disk resonator presented in Fig. 12. Fig. 17(b) does just this. Redrawing the circuit then yields the visually simpler version of Fig. 17(c) that better elucidates the series and parallel connected components. Here, it is no surprise that the core LCR elements modeling the vibrating disks cascade in series, since $\lambda/2$ -coupling forces the disks to vibrate in-phase with identical mode shapes. The result: Their dynamic stiffnesses, masses, and damping losses add linearly. Similarly, since the electrodes modeled by the transformers are in parallel, the forces exerted by the electrodes add cumulatively to generate a total combined force N_{io} times larger than that of a single electrode, where N_{io} is the number of driven input/output (I/O) electrodes, each fully surrounding a disk to the extent possible.

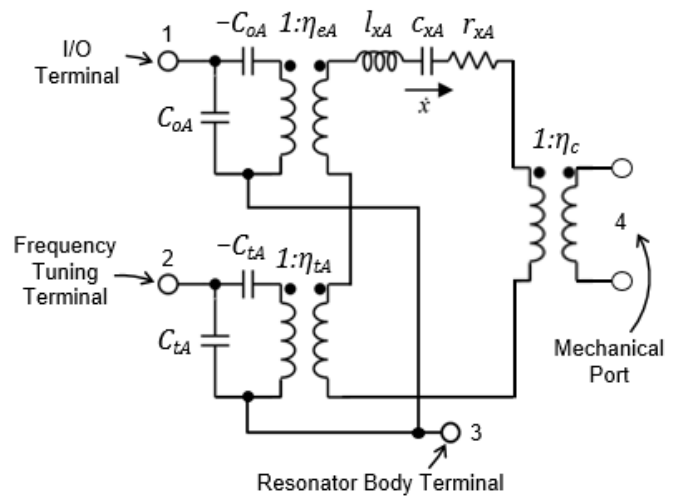


Fig. 18: General electrical equivalent circuit for the structure of Fig. 14.

Fig. 14 presents a more complex scenario, since some disks contribute to I/O, while others do not, as they might serve frequency tuning or other purposes; and any resonator may be used to mechanically couple to another mechanical structure, as indicated by the dashed beam on the right. The total effective equivalent circuit for an N_{io} -resonator $\lambda/2$ -coupled array-composite with N_{io} I/O disks, N_t tuning disks, and N_b buffer disks becomes that presented in Fig. 18, where expressions for the elements and turns ratios now take on the following forms:

$$\begin{aligned}
 \eta_{eA} &= N_{io} \times \eta_e \\
 \eta_{tA} &= N_t \times \eta_e \\
 r_{xA} &= N_{tot} \times r_x \\
 l_{xA} &= N_{tot} \times l_x \\
 c_{xA} &= \frac{1}{N_{tot}} \times c_x
 \end{aligned} \tag{28}$$

where η_{eA} and η_{tA} are the electromechanical coupling coefficients at the array-composite's input-output and tuning electrodes, respectively. Similarly, r_{xA} , l_{xA} , and c_{xA} represent the core- LCR values that model the equivalent damping, dynamic mass, and inverse dynamic stiffness of the array-composite, respectively. The mechanical coupler turns ratio η_c is 1 for the present case where mechanical couplers attach only at the edges of disks, but can be different from 1 when the velocity at the core or reference point for the LCR circuit differs from that at the coupling location [14], [15].

The Fig. 18 circuit shows four terminals: one that goes to the electrodes of all disks involved with I/O; one that goes to the electrodes of all disks intended for frequency tuning; one that goes to a mechanically coupled next stage; and one that goes to the movable structure. The circuit, of course, is general enough that many of the electrodes are re-assignable to other purposes at will.

C. Array-Composite Motional Resistance

With I/O electrodes in parallel and all disks vibrating in unison, the currents flowing into the I/O electrodes now add in phase, allowing for a total current N_{io} times that of a single electrode fully surrounding a single disk. Since the current increases for the same input voltage, the motional resistance of the structure decreases to

$$R_{xA} = \frac{N_{tot}}{N_{io}^2} R_x \quad (29)$$

where R_{xA} and R_x represent the motional resistance of the array-composite and a single disk resonator, respectively. The corresponding expression for the filter termination resistance follows from inserting (29) in (7) as

$$R_Q = \left(\frac{Q}{q_n Q_f} - 1 \right) \frac{N_{tot}}{N_{io}^2} R_x \cong \frac{Q}{q_n Q_f} \frac{N_{tot}}{N_{io}^2} \frac{r_x}{\eta_e^2} \quad (30)$$

where rewriting the single resonator's damping term r_x in terms of the resonator Q , dynamic mass m_m , and electromechanical coupling coefficient η_e leads to

$$R_Q = \frac{1}{Q_f} \frac{N_{tot}}{N_{io}^2} \frac{2\pi f_o m_m}{q_n \eta_e^2} \quad (31)$$

Rewriting m_m and η_e of (31) in terms of the fundamental design variables yields

$$R_Q = \frac{f_o}{Q_f} \frac{N_{tot}}{N_{io}^2} \frac{d_o^4}{V_P^2} \frac{2\pi^2 \chi \rho}{q_n h \varepsilon_o^2 \theta_{ov}^2} \quad (32)$$

The right-hand-most form of (30) addresses the specific case where the filter insertion loss is low, i.e., the resonator is Q much larger than the filter Q_f . In this case, the value of R_Q is independent of the unloaded resonator Q , and the knobs that best specify its value become the electrode-to-resonator gap spacing d_o (with a 4th power dependence) and the dc-bias voltage V_P (with a square-law dependence).

A single polysilicon disk resonating at 433 MHz with a Q of 20,000, 40-nm gaps, 26V dc-bias, thickness h of 3 μ m, and fully surrounding electrodes, i.e. $\theta_{ov}=2\pi$, would exhibit a motional resistance R_x of 364 Ω , which after assembly into a filter circuit is much too high to match to adjacent stages in a conventional receiver. In contrast, combination of 20 of these same resonators into a disk array-composite (with 12 I/O resonators, 8 buffers) with all I/O resonators hooked in parallel allows summation of output currents to reduce the motional resistance down to 50 Ω . According to (32), a two-resonator 0.1% bandwidth 0.5-dB-ripple Chebyshev filter using this array-composite requires a termination resistance of 470 Ω . Reducing gaps to 20-nm and dropping the dc-bias voltage to 9V reduces the needed number of array-composite resonators to 10 (with 6 I/O) to achieve the same filter response, but with an R_Q of 49 Ω .

Fig. 19 plots termination resistance R_Q versus number of 433-MHz based resonators in the array-composite for three different gap spacing examples of 80nm, 40nm, 20nm, and 10nm used in two- and three-resonator 0.5dB-ripple Chebyshev filters, showing the large range over which gap spacing and array size choices specify the filter termination resistance. Note that 10-nm gaps are not unreasonable, given recent demonstrations of 13-nm gaps [34].

D. Array-Composite Power Handling

In addition to motional resistance, the power handling of an array-composite improves over that of a single constituent resonator. This is obvious, given that the current now distributes among N_{io} devices, so any detrimental effects, e.g., heating, lessened by approximately the factor N_{io} .

Third-order intermodulation distortion is often a good gauge

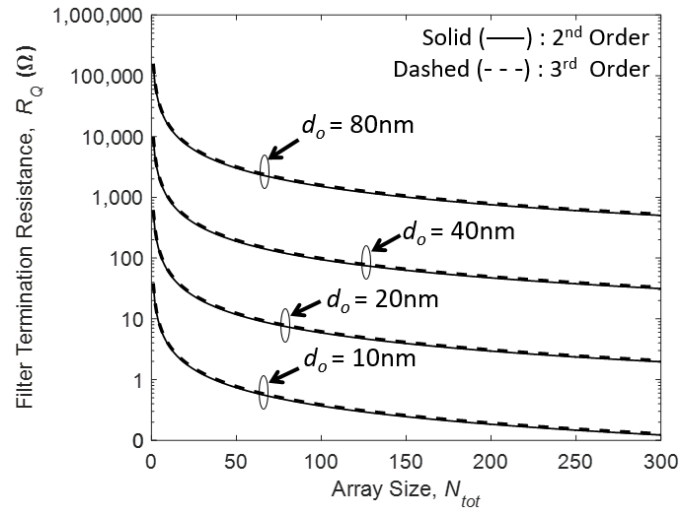


Fig. 19: Simulated plots of filter termination resistance vs. number of 433-MHz disk resonators in a half-wavelength-coupled array-composite calculated for three different gap spacing cases assuming two- and three-resonator 0.5dB-ripple Chebyshev filter designs. For these simulations, $V_P = 15V$, $h = 3\mu m$, $P_{BW} = 0.1\%$, $N_{tot} = N_{io}$, $\rho = 2300kg/m^3$, $\chi = 0.763$ (1st mode), $\theta_{ov} = 2\pi$, q_n (2nd order) = 1.9497, q_n (3rd order) = 1.8638. The curves show only small differences between 2nd and 3rd order.

for the largest input power acceptable to a given circuit element or system block. For practical applications, the third-order intermodulation intercept point IIP_3 , defined as the input power at which the output powers due to an input at the carrier frequency and at two frequencies equally spaced from it, i.e. $f_1 = f_o - \Delta f$ and $f_2 = f_o - 2\Delta f$, are equal, is a good metric for device or circuit linearity. [39] already developed an expression governing the IIP_3 of a radial-contour mode disk resonator, repeated here for convenience as follows [40] [25]:

$$P_{IIP_3} = P_{V^2X} \parallel P_{VX^2} \parallel P_{X^3} \quad (33)$$

This compact IIP_3 power expression comprises the parallel connection of three resonator non-linearity sources given by

$$\begin{aligned} P_{V^2X} &= \frac{4\pi\varepsilon_o f_o Q V_P^2 A_o}{d_o(2\Theta_1 + \Theta_2^*)} = \frac{4\pi\varepsilon_o f_o Q V_P^2 R h \theta_{ov}}{d_o(2\Theta_1 + \Theta_2^*)} \\ P_{VX^2} &= \frac{4\pi f_o Q d_o^2 k_{re}}{3\Theta_1(\Theta_1 + 2\Theta_2^*)} = \frac{16\pi^4 f_o^3 Q d_o^2 R^2 h \chi \rho}{3\Theta_1(\Theta_1 + 2\Theta_2^*)} \\ P_{X^3} &= \frac{2\pi f_o Q d_o^5 k_{re}^2}{3\varepsilon_o A_o V_P^2 \Theta_1^2 \Theta_2^*} = \frac{32\pi^7 f_o^5 Q d_o^5 R^3 h \chi^2 \rho^2}{3\varepsilon_o \theta_{ov} V_P^2 \Theta_1^2 \Theta_2^*} \end{aligned} \quad (34)$$

where starred variables indicate complex conjugates, A_o is the overlap area between the electrode and the disk, k_{re} is the effective stiffness of a single disk at the edge, Θ_1 and Θ_2 model the degree to which the resonator's amplitude transfer function attenuates the blocker input tones and take the form

$$\begin{aligned} \Theta_1 &= \frac{1}{1 - (f_1/f_o)^2 + j(f_1/Qf_o)} \\ \Theta_2 &= \frac{1}{1 - (f_2/f_o)^2 + j(f_2/Qf_o)} \end{aligned} \quad (35)$$

Here, the P_{V^2X} and P_{VX^2} terms derive from nonlinear interactions between voltage and displacement, while the P_{X^3} term is purely displacement-derived.

For an array-composite like that of Fig. 14 with N_{io} I/O electrodes and N_{tot} electrodes, the expression for IIP_3 becomes

$$P_{IIP_3} = N_{tot} \left[\beta P_{V^2X} \parallel P_{VX^2} \parallel \frac{P_{X^3}}{\beta} \right] \quad (36)$$

where $\beta = N_{io}/N_{tot}$. If all disks are I/O disks, then the improvement in IIP_3 becomes linear with N_{tot} .

E. Array-Based Mechanical Impedance Tailoring

Equation (29) already showed how the number of resonators N_{tot} used in a mechanically coupled array-composite acts as a knob to control the electrical resistance presented by any one (or group) of its resonators. Note further that coupling all resonators in this way does more than merely add together currents to lower electrical motional impedance and raise power handling. In fact, one of the most useful characteristics of an array-composite for filter design is the degree to which it can tailor the mechanical impedance, i.e., as governed by the effective stiffness and mass, presented to a mechanical input/output port.

The amount of stiffness tailoring available is readily apparent when determining the impedance seen into the mechanical port in the array-composite equivalent circuit of Fig. 18 with the other ports grounded. In particular, grounding terminals 1, 2, and 3 of this circuit leaves port 4 essentially coupled to an effective resonator with mass, stiffness, and damping values all N_{tot} times as large as that of a single resonator. This means the stiffness presented to a mechanical structure, e.g., a coupling beam, attached to a disk's edge, is N_{tot} times as large as that of a single disk resonator. Thus, N_{tot} acts as a knob to control the mechanical impedance presented by any one of its resonators.

As will be seen, the dynamic stiffness presented at a coupling location very much controls the bandwidth of a given filter design. The ability to raise the presented stiffness by arraying equates to an ability to decrease the percent bandwidth of a given filter, such as needed for RF channel-selection.

IX. MINIMUM ELECTROMECHANICAL COUPLING STRENGTH REQUIRED FOR THE CHOSEN BANDWIDTH

Although array size strongly influences the impedance presented by the combined array-composite input terminal, it does not raise the electromechanical coupling strength gauged by the ratio of motional-to-static input capacitance (C_{xA}/C_{oA}). For the case where all disks possess I/O electrodes and all electrodes are hooked in parallel, i.e. $N_{tot} = N_{io}$, (C_{xA}/C_{oA}) follows readily by simply taking the ratio of

$$C_{xA} = N_{tot} \eta_e^2 c_x = N_{tot} \frac{V_P^2 h(\epsilon_o R \theta_{ov})^2}{d_o^4 \pi^3 \chi K_{mat}^2 E} \quad (37)$$

and

$$C_{oA} = N_{tot} C_o = N_{tot} \frac{\epsilon_o R \theta_{ov} h}{d_o} \quad (38)$$

which yields

$$\frac{C_{xA}}{C_{oA}} = \frac{V_P^2}{d_o^3} \frac{\epsilon_o R \theta_{ov}}{\pi^3 \chi K_{mat}^2 E} \quad (39)$$

Here, (C_{xA}/C_{oA}) does not change with the number of I/O disks.

If, on the other hand, non-I/O disks are included, as described in Section I, the expression for electromechanical coupling strength becomes

$$\frac{C_{xA}}{C_{oA}} = \frac{N_{io}}{N_{tot}} \frac{V_P^2}{d_o^3} \frac{\epsilon_o R \theta_{ov}}{\pi^3 \chi K_{mat}^2 E} \quad (40)$$

where N_{tot} is the total number of mechanically coupled disks that include both the I/O and non-I/O disks, which means the N_{io}/N_{tot} term in (40) is always less than one. In (40), the only other adjustable variables are V_P and d_o , as the rest are fixed by the chosen center frequency f_o . In most practical cases, it is up to the dc-bias V_P and electrode-to-resonator gap d_o scaling to insure adequate electromechanical coupling (C_{xA}/C_{oA}) to meet the requirement of (3) [24].

To gauge how the minimum C_{xA}/C_{oA} that avoids passband distortion for a given filter bandwidth B scales with frequency, one can use (21) and (40) to rewrite (3) as

$$\frac{1}{B} \left(\frac{V_P^2}{d_o^3} \right) \left(\frac{\epsilon_o \theta_{ov} N_{io}}{2\pi^3 \chi K_{mat} N_{tot} \sqrt{E\rho}} \right) > \gamma \quad (41)$$

The terms in the rightmost parentheses in (41) comprise material, resonator, and filter design constants that are fixed for a given filter response and technology choice. This again leaves the bias voltage V_P and electrode-to-resonator gap spacing d_o as the primary design knobs to satisfy (41) for a given desired bandwidth B . It is important to observe that (41) is independent of disk radius, and thus, of the filter center frequency f_o . Thus, if the needed bandwidth stays constant for a bank of filters over a range of frequencies—which is often the case for RF channel-selection—then so do the needed gap d_o and bias voltage V_P for each filter in the bank.

X. FILTER PASSBAND SPECIFICATION

Section IV described how mechanical coupling of two identical single disk resonators—or more preferably identical array-composites that behave as single disks with reduced R_x —creates a two degree of freedom system with two closely spaced modes that define a filter passband, as described in Fig. 9. A more explicit expression for the bandwidth of the filter follows from (10), which accounting for the stiffness transformation afforded by arraying described by (28), yields

$$B = \frac{k_{c,ij} f_o}{k_{reA} k_{ij}} = \frac{k_{c,ij}}{k_{re}} \frac{f_o}{N_{tot} k_{ij}} \quad (42)$$

where k_{reA} is the effective stiffness of a disk array-composite, and $k_{c,ij}$ is the stiffness of the filter coupling beam between i^{th} and j^{th} resonators in a multi-resonator filter. While any coupling beam length can be chosen to provide the dynamic stiffnesses $k_{c,ij}$ for the required filter bandwidth in (42), beams with lengths matching odd multiples of the quarter-wavelength, i.e. $\lambda/4$, form a special case that minimizes the sensitivity of the filter response to variations in beam dimensions, e.g., caused by finite fabrication tolerances. This resilience against process variations arises from the fact that $\lambda/4$ dimensions zero out the derivative of the dynamic beam stiffness with respect to the beam length [38].

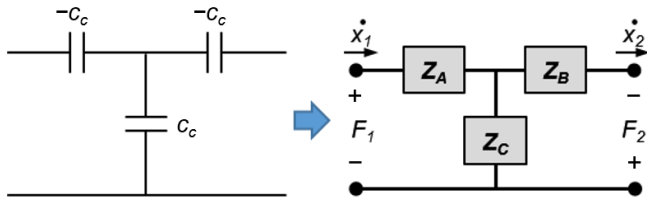


Fig. 20: Transmission line model equivalent of the $\lambda/4$ beam electrical equivalent circuit.

A. Electrical Equivalent Circuit for a $\lambda/4$ Coupling Beam

Like other components of a mechanical filter, the behavior of a $\lambda/4$ coupling beam follows the prediction of its equivalent electrical circuit. As described in Section VIII, the characteristics of a small cross-section coupling beam vibrating in its extensional mode are similar to the behavior of an electrical transmission line, and in $ABCD$ matrix form conform to (23). The special case of a quarter-wavelength coupling beam with $l_c = \lambda/4$ sets the electrical length of the transmission line equivalent representation of the beam to $\beta l_c = \pi/2$ in (23), which then yields the $ABCD$ matrix expression for a $\lambda/4$ coupling beam

$$\begin{bmatrix} F_1 \\ \dot{x}_1 \end{bmatrix} = \begin{bmatrix} 0 & jY_o \\ jZ_o & 0 \end{bmatrix} \begin{bmatrix} F_2 \\ \dot{x}_2 \end{bmatrix} \quad (43)$$

Here, the $\lambda/4$ coupling beam behaves as an impedance inverter commonly used in ladder filter design [41].

As introduced in Section IV, a T -network of capacitors (*cf.* Fig. 9) aptly captures the electrical equivalent lumped circuit model of the $\lambda/4$ coupling beam. Fig. 20 presents the transmission line representation of this circuit, where Z_A , Z_B , and Z_C model the series and shunt arm impedances. Equating the $ABCD$ matrices of the circuit presented in Fig. 20 [41] with that of (43) leads to

$$\frac{1}{Z_c} = jZ_o \rightarrow j\omega_o c_c = \frac{j}{hw_c \sqrt{\rho E}} \quad (44)$$

which then yields the expression for the dynamic stiffness of a $\lambda/4$ coupling beam in terms of beam dimensions:

$$k_c = \frac{1}{c_c} = \frac{\pi E hw_c}{2 l_{\lambda/4}} \quad (45)$$

where w_c is the width of the coupling beam, and $l_{\lambda/4}$ is the beam length equal to

$$l_{\lambda/4} = \frac{\xi}{4f_o} \sqrt{\frac{E}{\rho}}, \quad \xi = 1, 3, 5, \dots \quad (46)$$

where the presence of ξ indicates that any odd multiple of the quarter-wavelength also provides the desired variance resilience.

B. $\lambda/4$ Coupling Beam Width & Array Size

Inserting (25) and (45) in (42) provides the filter bandwidth expression in terms of fundamental device geometry and material properties:

$$B = \frac{w_c}{N_{tot}} \left(f_o^2 \frac{2}{\xi \pi^2 K_{mat}^2 \chi k_{ij}} \sqrt{\frac{\rho}{E}} \right) \quad (47)$$

The only free variables to set the filter bandwidth B in (47) are

the $\lambda/4$ beam width w_c and the array size N_{tot} , where the remaining terms given in the parentheses are fixed by other filter specifications.

It is important to observe from (47) that very small bandwidths may require excessively narrow beam widths. This becomes especially true if the array-composite design approach is not used, i.e. if $N_{tot}=1$. Interestingly, use of array-composites with large enough N_{tot} becomes critical to maintaining w_c wider than the critical dimension $w_{c,min}$ that can be reliably manufactured, as governed by

$$w_c = N_{tot} \left(\frac{B}{f_o} \right) \frac{\xi \pi^2 K_{mat}^2 \chi k_{ij}}{2f_o} \sqrt{\frac{E}{\rho}} > w_{c,min} \quad (48)$$

Taking as an example the 433-MHz disk resonator of Section VIII.C, the use of stand-alone polysilicon disk resonators to form a second order Chebyshev filter with 0.5dB ripple not only demands an impractically high termination resistance (exceeding 10k Ω), but also requires a very narrow $\lambda/4$ coupling beam width of 22nm with $k_{ij}=0.7225$ and $N_{tot}=1$ in (48). Here, increasing the array size to $N=24$ adjusts the beam width to $w_c = 534$ nm that can now be reliably patterned and etched into 3 μ m-thick polysilicon using DRIE, with the added benefit of low sub-1k Ω filter termination resistances. So arraying is critical to successful filter realization.

Equation (48) further indicates that filters with very small fractional bandwidth $P_{BW} = B/f_o$, such as needed for RF channel-selection [7], must use resonator array-composites with size N_{tot} greater than a minimum number N_{min} set by $w_{c,min}$ according to

$$N_{tot} \geq N_{min} = \frac{w_{c,min}}{P_{BW}} \frac{2f_o}{\xi \pi^2 K_{mat}^2 \chi k_{ij}} \sqrt{\frac{\rho}{E}} \quad (49)$$

regardless of other filter specifications such as filter termination resistance or layout area. Fig. 21 uses (49) to plot the minimum achievable fractional bandwidth P_{BW} for a 2nd order polysilicon Chebyshev filter operating at 1GHz for different minimum filter coupling beam widths. These curves demonstrate the wide fractional filter bandwidth range achievable by mechanically coupled disk filters, where larger array sizes enable smaller fractional bandwidths desired for channel-select applications.

The large number of $\lambda/2$ coupled disks indicated in Fig. 21 may at first glance raise area and cost concerns; however, the disks that form the array have tiny dimensions that scale inversely proportional to frequency. For example, a 0.1% fractional bandwidth 2nd order polysilicon filter operating at 1GHz with 0.25 μ m wide coupling beams requires $N_{tot}=25$ $\lambda/2$ coupled resonators per array-composite. As illustrated in Fig. 2, a second order differential filter comprises four array-composites, which in this case leads to $N_{tot}=25$ resonators in each quadrant. This 100-coupled disk resonator circuit would consume only 110 μ m \times 110 μ m die area (assuming electrode routing is done in another layer as in CMOS), where each disk has a diameter of only 5.4 μ m. To put this tiny footprint in perspective, one could amass 2,025 similar filters on a 5mm \times 5mm chip, perhaps towards devising a low cost, programmable mode-selectable RF channelizing filter bank for a very flexible receiver front-end capable of satisfying nearly any communication standard.

Though this paper focuses on channel-selecting filters, note that larger bandwidth filters, e.g., 3% for band-selection, can employ multiple wider coupling beams to raise the spring-to-

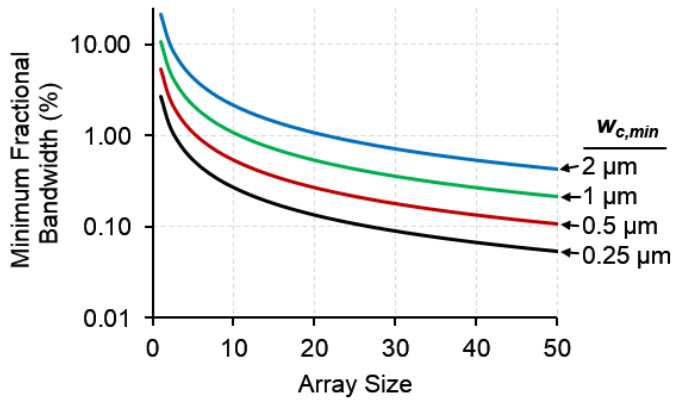


Fig. 21: Simulated curves of minimum achievable fractional bandwidth as a function of array size for different minimum coupling beam widths for a 2nd order polysilicon Chebyshev filter operating at 1GHz.

resonator array-composite ratio.

XI. DIFFERENTIAL MECHANICAL DESIGN

A differential filter with electrically and mechanically symmetric drive and sense has two advantages over a single-ended one:

- 1) Symmetric (i.e., differential) design suppresses spurious modes close to the filter center frequency generated by complex mechanical circuit non-idealities [19].
- 2) Common-mode feedthrough currents flowing through parasitic elements, e.g., capacitors formed by electrode-disk overlaps and substrate couplings, cancel.

Much like differential transistor pair design, if the micromechanical resonator circuit could encompass two symmetric halves forced to resonate at the same vibration frequency but 180° out of phase, this would yield the desired differential operation with the stated benefits. Similar to the analysis presented in Section VIII for $\lambda/2$ beams that enforce in-phase vibration, the electrical transmission line analogy outlined by (23) also reveals the coupling beam design needed to enforce differential vibration. Here, setting the beam length l_c to the full wavelength λ so that the electrical length becomes $\beta l_c = \beta \lambda = 2\pi$ yields the ABCD matrix

$$\begin{bmatrix} F_1 \\ \dot{x}_1 \end{bmatrix} = \begin{bmatrix} 1 & 0 \\ 0 & 1 \end{bmatrix} \begin{bmatrix} F_2 \\ \dot{x}_2 \end{bmatrix}, \quad F_1 = F_2, \quad \dot{x}_1 = \dot{x}_2 \quad (50)$$

With reference to Fig. 22(a), the $\dot{x}_1 = \dot{x}_2$ condition in (50) is only possible when one of the coupled disks contracts while the other expands to keep the displacement magnitude and direction on both ends of the coupling beam identical. As a result, λ -coupled disks assume the same vibration frequency but out-of-phase displacement.

Similar to Fig. 16 that explains the in-phase $\lambda/2$ coupler model, Fig. 22 illustrates the equivalent circuit model for the full-wavelength differential coupler. Here, the width of the λ differential coupler does not change its network properties at resonance, much like the $\lambda/2$ coupler, and typically equals the minimum critical dimension to avoid loading the disk resonators by unnecessarily wide coupling beams.

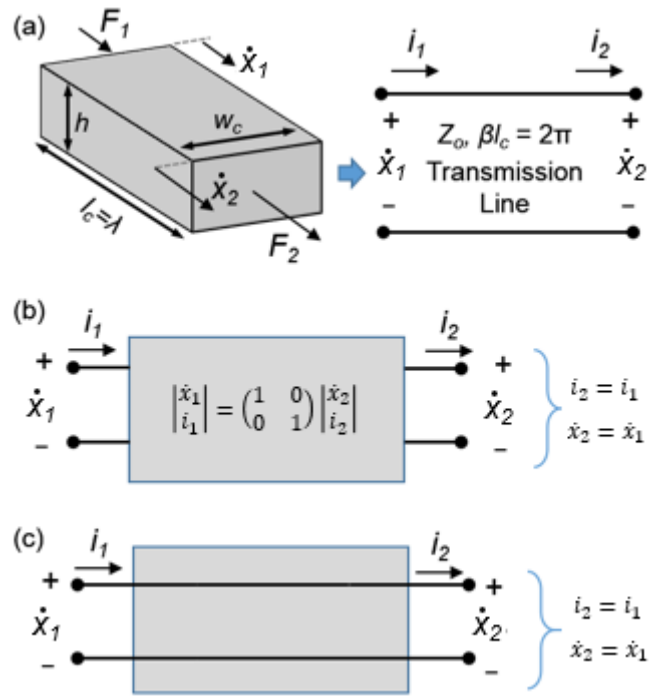


Fig. 22: (a) Schematic view of a λ extensional-mode coupling beam and its acoustic transmission equivalent representation with acoustic impedance Z_0 and electrical length $\beta l_c = 2\pi$. (b) ABCD matrix representation for the acoustic transmission line formed by the λ beam. (c) Electrical equivalent circuit representation of the λ beam.

Fig. 23 illustrates the electrical equivalent circuit for a λ -coupled differential disk pair, which combines the equivalent circuit of a single disk resonator given by Fig. 12 and the circuit model for the λ coupler given by Fig. 22(c). Similar to the $\lambda/2$ coupled case presented in Fig. 17(c), the core-*LCR* circuits of the λ -coupled disks add in series. However, in contrast to the $\lambda/2$ coupled case, the electrodes of the λ -coupled pair combine in parallel with differential polarity. Therefore, the electrodes must drive differentially, i.e. with 180° phase difference relative to each other, to avoid cancelling the motional currents generated by the individual disks.

A. Differential Filter Topology

To convey how the overall differential filter structure functions, Fig. 24 presents the expected properly terminated filter frequency response for a simplified 4-disk-array version of this design, with dotted lines to show its unterminated response, and with FEA-simulated vibration mode shapes corresponding to each peak of the response. Here, the $\lambda/2$ beams combine four disk resonators in each quadrant to create four array-composites that act like four single disks, but with $4\times$ less R_r . Note how all disks in a given array-composite vibrate with the same phase and mode shape—a result of $\lambda/2$ -coupling.

To induce differential operation, λ -coupling of the array-composites in the upper and lower halves of the mechanical circuit enforces out-of-phase motion between left-half top and bottom array-composites (which comprise the input devices) and right-half ones (comprising the output devices). Fig. 24 clearly shows how the upper and lower array-composites in the left and right halves move with opposite phase when the whole structure

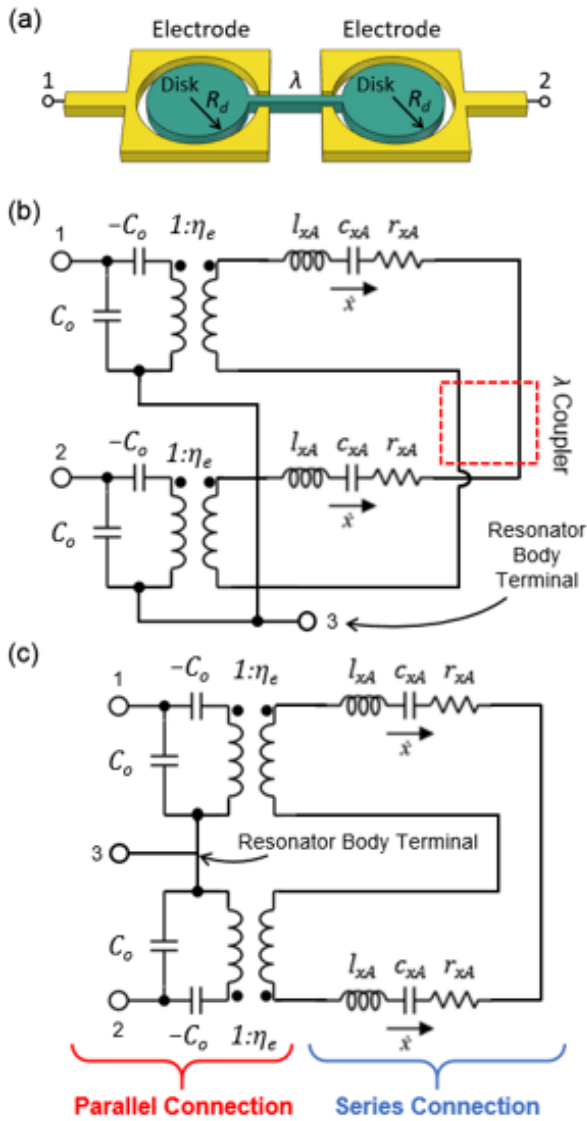


Fig. 23: (a) Schematic view of a two-resonator network coupled by a full-wavelength beam. (b) Electrical equivalent circuit representation of the two-resonator differential array-composite that combines the circuits presented in Fig. 12 and Fig. 22(c); and (c) the same circuit after combining series elements.

vibrates, no matter the mode. A consequence of this is that (ideally) common-mode input forces cannot excite this filter; only differential ones within the passband can, which means only differential signals can pass through the structure.

To maintain symmetry, $\lambda/4$ beams connect the left and right differential array-composites, serving to split their frequencies to form peaks that define the filter passband. In particular, the mode that actuates the $\lambda/4$ beams the least generates the low frequency peak, *cf.* Fig. 24(a); while the mode that flexes these couplers the most specifies the high frequency one, *cf.* Fig. 24(b). Upon filter termination, loading of the resonators widens their frequency response spectra, allowing them to add constructively between peaks and subtract outside, yielding the desired filter response.

The filter response simulations in Fig. 24 are not only consistent with Fig. 10's depiction of passband flattening via termination, it further more accurately depicts the reduction of insertion loss expected when one properly terminates a filter [14].

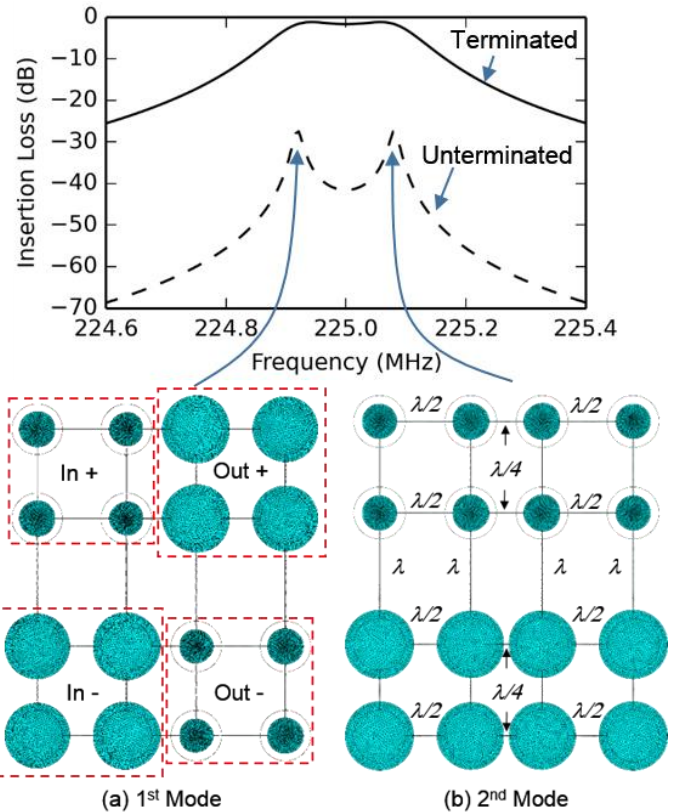


Fig. 24: FEA simulation of mode shapes of disk resonators coupled by various wavelength optimized beams, where λ -coupling enforces differential vibration of upper and lower halves, and $\lambda/4$ beams realize (a) out-of-phase (lower frequency 1st mode) and (b) in-phase (higher frequency 2nd mode) filter modes. Here, the terminated filter plot simulation used $R_Q = 600\Omega$ (i.e., the design value of Part II), while the unterminated plot used $R_Q = 10\Omega$.

In essence, the termination resistors R_Q serve as source and load resistors. The bigger they are, the less attenuation by the finite filter resistance, so the smaller the insertion loss. Of course, they should not be larger than the filter design value, since this would introduce undue peaking in the passband, compromising its flatness.

XII. FILTER ELECTRICAL EQUIVALENT CIRCUIT MODEL

Much like their transistor circuit counterparts, the design of micromechanical circuits benefits immensely from behavioral models that capture their electrical response in circuit simulators, such as SPICE [42]. It is to this end that previous sections employed electromechanical analogies to capture the functionality added by each level of hierarchy. The overall filter equivalent circuit combines these sub-circuits as modules and accurately captures the filter electrical behavior for arbitrary terminations.

Fig. 25(b) presents the electrical equivalent circuit for the 2nd order differential filter of Fig. 25 (a), which is simpler than that of Fig. 2 for illustrative purposes. Here, each five-resonator $\lambda/2$ -coupled array-composite equates to a circuit similar to that of Fig. 18(b). Here, $N_{io}=2$ in (28), since only two electrodes in each array-composite bear I/O electrodes, the third reserved for frequency tuning. Buffer devices to alleviate stress-related issues mentioned earlier in Section I and detailed more extensively in

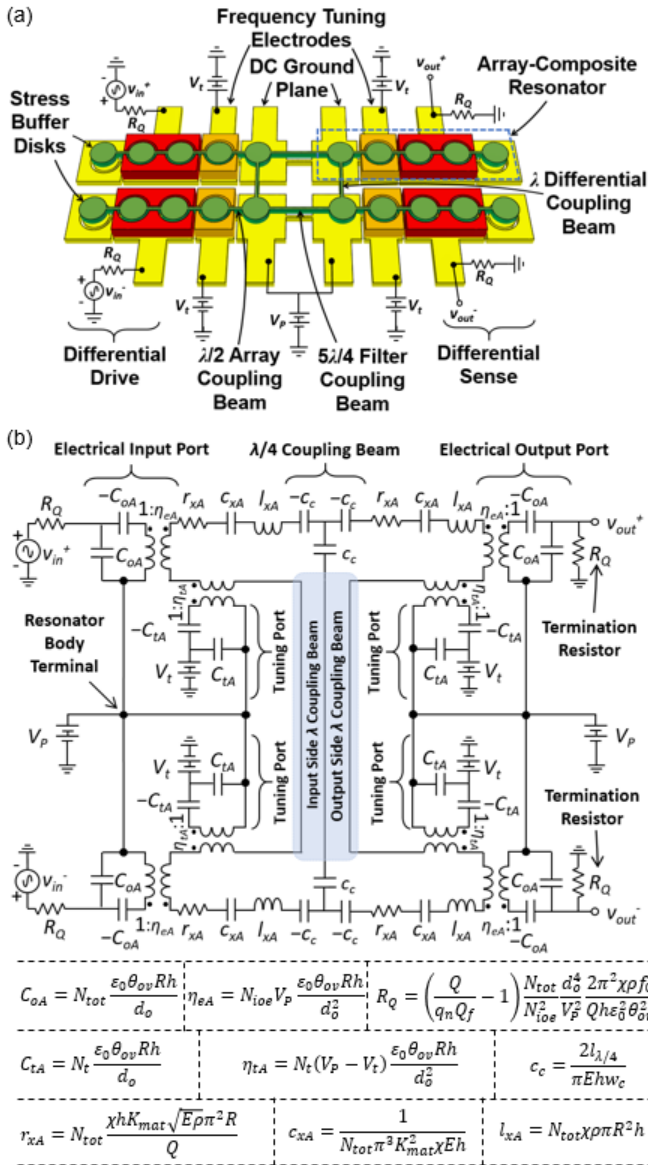


Fig. 25: (a) Schematic description of a 2nd order differential filter. (b) Electrical equivalent circuit for a 2nd order differential filter.

Part II, Section II also book-end each array. The $\lambda/4$ filter coupling beams that adjoin the upper and lower array-composites equate to T -networks like that of Fig. 20. Finally, the differential operation imposed by the λ coupling beams between upper and lower array-composites is captured by the electrically balanced differential drive and sense for the symmetric upper and lower half-circuits presented in Fig. 25.

Note that the corresponding circuit for the design of Fig. 2 is identical to that for Fig. 25(a), except that N_{io} is 14, and N_{oi} is 24.

XIII. FILTER DESIGN PROCEDURE

Table III presents a procedure for designing a complete filter in the topology of Fig. 2 alongside example design values that illustrate the design of the actual filter demonstrated in Part II. As is often the case with complex circuit designs, there is no one solution that achieves a given filter specification, but rather several valid solutions, where which one ensues depends upon

choices made during the design process. The design process thus becomes an exercise in making choices that optimize a given desired outcome, e.g., smallest size, most tunable, etc. Thus, this section focuses on guidelines for choosing appropriate initial values. The design procedure of Table III does just this.

Any design of course begins with a specification. For a filter, this includes the center frequency f_o , bandwidth B , type (e.g., Chebyshev, Butterworth, etc., essentially specified by k and q values [29]), order, desired termination resistance R_Q , and the structural material set that specifies material constants and Q . Table I of Part II includes these specifications for the demonstrated 224-MHz filter of Part II.

Given the hierarchical nature of the Fig. 2 circuit, it makes sense to start with the base device, i.e., the disk resonator, then work to build the larger circuit. Design of the disk essentially boils down to determining its radius assuming (for now) no applied voltages, which simplifies things by removing consideration of electrical stiffness. Once known, the disk radius yields its dynamic mass and stiffness. For the demonstrated 224-MHz design of Part II, the radius, mass, and stiffness are 12.1 μ m, 2.42 $\times 10^{-12}$ kg, and 4.79MN/m, respectively.

At this point, one must start making choices. The first things to choose are the electrode-to-resonator gap spacing d_o and the dc-bias voltage V_p . Each of these variables comes with constraints: manufacturing constraints for the former and breakdown or pull-in constraints for the latter. One good approach is to just choose a gap spacing, e.g., 40nm, and then let the (C_x/C_o) spec govern the dc-bias voltage. A good rule of thumb here is to choose a d_o and V_p combination that yields a (C_x/C_o) about 1.5 γ times the filter fractional bandwidth (γ from (3)). For the Part II filter, the intended d_o of 40nm leads to an initial V_p choice of 16V. If the needed V_p ends up too high, then reductions in d_o can help to lower V_p .

The next most logical design parameter to choose is the number of resonators in each of the four $\lambda/2$ -coupled array-composite quadrants. Assuming a symmetric design like that of Fig. 2, this comes down to choosing the number of rows N_{row} and columns N_{col} of disks and ultimately the number of disks used for I/O, tuning, and stress buffering in each quadrant. Here, one should start by simply choosing the number of rows. Since each row associates with two buffers in the Fig. 2 design, i.e., $N_b = 2N_{row}$, the smaller the number of rows chosen, the smaller the array. Choosing only one row per quadrant, however, makes for a long and thin filter for which long distances between disks might worsen fabrication mismatch issues. Choosing a larger number of rows makes for a more compact square-like quadrant, leading to a filter shape like Fig. 2, while also providing more points at which $\lambda/4$ coupling beams might be placed (in parallel) for larger bandwidth designs. But at the cost of more resonators. The chosen number of rows is 4 for the Part II filter, which Fig. 2 in this part depicts in an illustration.

Determination of the number of columns requires first the number of I/O resonators needed to insure the termination resistance value R_Q . The number of I/O resonators needed follows

TABLE III: FILTER DESIGN PROCEDURE WITH EQUATIONS

<p>Given the following parameters: <u>Design Goals:</u> f_o, B, R_Q <u>Filter Constants:</u> q_n, k_{ij}, γ <u>Resonator & Material Constants:</u> $Q, E, \rho, K_{mat}, \theta_{ov}, \chi, \sigma_{single}^*$ <u>Dimension Constraints:</u> $w_{c,min}, d_o, h$ <u>Voltage Constraints:</u> V_{max}^\ddagger</p> <p><u>Find:</u> $R, N_{tot}, N_{io}, N_t, V_p, \lambda, w_c$.</p> <ol style="list-style-type: none"> Find the disk radius R using (51). Solve (52) for V_p to achieve sufficient C_x/C_o with corresponding γ value from Table I. Pick the number of rows N_{row} in a quadrant. Use (53) to determine the number of I/O electrodes needed for R_Q. Assume $N_t = 0$ for now. Use (54) to determine the number of columns N_{col}. If σ_{single} is known, use (55) and (56) to determine the minimum number of tuning electrodes for the desired yield. If needed, increment V_p or N_{col}. Determine R_Q using (57). Adjust V_p or N_{col} to match the spec, if needed. Use (58) to confirm correct center frequency after arraying. Determine the acoustic wavelength λ by (59) for the $\lambda/4$ filter, $\lambda/2$ array-composite, and λ differential couplers. Determine the coupling beam dimension w_c that meets the desired filter bandwidth B specification using (60). Assemble the fully balanced structure of Fig. 2. Use (61)-(64) to generate the equivalent circuit of Fig. 25, then simulate to confirm the correct filter response. 	Mechanical Design Variables	Disk Radius $R = \frac{K_{mat}}{2f_o} \sqrt{\frac{E}{\rho}}$	(51)
		Approx. Required Bias Voltage for Sufficient Array C_x/C_o $V_p^2 \geq 1.5\gamma \frac{P_{BW} k_m d_o^3}{\epsilon_o A_o} = 1.5\gamma d_o^3 \frac{2B\pi^3 \chi K_{mat} \sqrt{E\rho}}{\epsilon_o \theta_{ov}}$	(52)
		Total No. of Disks to Attain Spec'ed Termination Impedance R_Q $N_{io} = \frac{\Gamma}{2} + \sqrt{\left(\frac{\Gamma}{2}\right)^2 + \Gamma N_b}$ where $\Gamma = \frac{2\pi B m_m}{q_n \eta_e^2 R_Q} = \frac{\pi \chi \rho \omega_o}{Q_f q_n h \epsilon_o^2 \theta_{ov}^2 R_Q V_p^2}$, $N_b = 2N_{row}$	(53)
		No. of Columns Needed $N_{col} > \frac{N_{io} + N_b}{N_{row}}$	(54)
		No. of Tuning Electrodes $N_t = N_{col} N_{row} - N_{io} - N_b$	(55)
		No. of Tuning Electrodes Needed for % Perfect-Tuned Yield [‡] $N_t \geq i \sigma_{single} \frac{\sqrt{2N_{tot} k_m d_o^3}}{\epsilon_o A_o V_T (2V_p - V_T)} = i \sigma_{single} \frac{\sqrt{2N_{tot} \pi^3 K_{mat}^2 \chi E d_o^3}}{\epsilon_o \theta_{ov} R V_T (2V_p - V_T)}$ where $i = 1$ (68.3%), 2 (95.4%), 3 (99.7%), ...	(56)
		Termination Impedance R_Q $R_Q = \left(\frac{Q}{q_n Q_f} - 1\right) \frac{N_{tot} r_x}{N_{io}^2 \eta_e^2} = \left(\frac{Q}{q_n Q_f} - 1\right) \frac{\omega_o N_{tot} d_o^4}{Q N_{io}^2 V_p^2 h \epsilon_o^2 \theta_{ov}^2} \frac{\pi \chi \rho}{h}$	(57)
		Array Quadrant Center Frequency $f_o = \frac{1}{2\pi} \sqrt{\frac{k_m}{m_m}} \sqrt{1 - \frac{\epsilon_o A_o}{d_o^3 k_m} \left\{ \frac{N_{io} V_p^2}{N_{tot}} - \frac{N_t}{N_{tot}} (V_p - V_T)^2 \right\}}$	(58)
		Wavelength for Coupling Beam Designs $\lambda = \frac{1}{f_o} \sqrt{\frac{E}{\rho}}$	(59)
		$\lambda/4$ Coupling Beam Width to Attain Filter Bandwidth B $w_c = N_{tot} \frac{B m_m}{h} \frac{2\pi \xi k_{ij}}{\sqrt{E\rho}} = \frac{\xi N_{tot} \pi^2 K_{mat}^2 \chi k_{ij} P_{BW}}{2f_o} \sqrt{\frac{E}{\rho}}$ where $\xi = 1, 3, 5, \dots$	(60)
Filter Electrical Equivalent Circuit Elements	$\lambda/4$ Coupling Beam Lumped Element $C_c = \frac{2(\xi\lambda/4)}{\pi E h w_c} = \frac{\xi}{h w_c \omega_o \sqrt{E\rho}}$ where $\xi = 1, 3, 5, \dots$	(61)	
	Array-Composite Core-LCR Elements $r_{xA} = N_{tot} \frac{m_m \omega_o}{Q} = N_{tot} \frac{\chi h K_{mat} \sqrt{E\rho} \pi^2 R}{Q}$ $l_{xA} = N_{tot} m_m = N_{tot} \chi \rho \pi R^2 h$ $C_{xA} = \frac{1}{N_{tot} m_m \omega_o^2} = \frac{1}{N_{tot} \pi^3 K_{mat}^2 \chi E h}$	(62)	
	I/O Electrode Elements $\eta_{eA} = N_{io} V_p \frac{\epsilon_o \theta_{ov} R h}{d_o^2}$ $C_{oA} = N_{io} \frac{\epsilon_o \theta_{ov} R h}{d_o}$	(63)	
	Tuning Electrode Elements $\eta_{tA} = N_t (V_p - V_T) \frac{\epsilon_o \theta_{ov} R h}{d_o^2}$ $C_{tA} = N_t \frac{\epsilon_o \theta_{ov} R h}{d_o}$	(64)	

* σ_{single} is the single disk resonator's frequency standard deviation.

‡ V_{max} is the maximum voltage allowed in the technology.

‡‡ Derived in Part II of this paper. Assumes $V_T = V_p$ for maximum tuning.

TABLE IV: 2ND ORDER DIFFERENTIAL CHEBYSHEV POLYSILICON DISK FILTER BANK DESIGN EXAMPLE[†]

Filter Specifications				Computed Quadrant Design Variables													
f_o (MHz)	B (kHz)	PBW (%)	IL (dB)	$Min.$ $Req. Q$	V_P (V)	C_x/C_o (%)	d_o (nm)	R_Q (Ω)	R (μm)	$l_{\lambda/4}$ (μm)	w_c (nm)	N_{tot}	N_{io}	N_t	Array Size (row x col)	Area ($\mu\text{m} \times \mu\text{m}$)	Area (mm^2)
50	30	0.060	2	15,957	5	0.372	20	46	54.2	41.4	1850	16	11	1	2×8	300×1450	0.434
100	30	0.030	2	31,915	5	0.186	20	46	27.1	20.7	463	16	11	1	2×8	150×724	0.108
250	500	0.200	2	4,787	9	0.275	20	49	10.8	8.29	4630	60	47	1	6×10	213×366	0.0780
433	500	0.115	2	8,291	9	0.143	20	50	6.26	4.79	1852	72	51	3	9×8	189×167	0.0316
700	500	0.071	2	13,404	9	0.089	20	50	3.87	2.96	708	72	51	5	8×9	103×117	0.0121
900	500	0.056	2	17,234	9	0.071	20	48	3.01	2.30	416	70	51	5	7×10	69×102	0.0071
1200	1000	0.083	2	11,489	12	0.104	20	48	2.26	1.73	435	65	52	3	5×13	36×100	0.00365
1800	1000	0.056	2	17,234	12	0.067	20	48	1.51	1.15	208	70	54	2	7×10	35 x 51	0.00177
2400	1000	0.042	2	22,978	12	0.050	20	48	1.13	0.86	117	70	54	2	7×10	26×38	0.00100
3000	1000	0.033	2	28,723	12	0.035	20	49	0.90	0.69	75	70	52	4	7×10	21×30	0.00064

[†] Assumes $h=3\mu\text{m}$, $\theta_{ov}=330^\circ$, and fundamental mode resonance.

TABLE V: 2ND ORDER DIFFERENTIAL CHEBYSHEV POLYSILICON DISK FILTER BANK EQUIVALENT CIRCUITS

Filter Specifications				Equivalent Circuit Element Values								
f_o (MHz)	B (kHz)	PBW (%)	IL (dB)	R_Q (Ω)	C_{oA} (pF)	η_{eA} ($\mu\text{C}/\text{m}$)	r_{xA} ($\mu\Omega$)	c_{xA} (nF)	l_{xA} (pH)	c_c (μF)	C_{tA} (pF)	η_{tA} (C/m)
50	30	0.060	2	46	4.56	1,140	15.30	13.049	777.27	30.10	0.414	0
100	30	0.030	2	46	2.28	567	3.82	13.049	194.32	60.20	0.207	0
250	500	0.200	2	49	3.90	1753	38.24	3.480	116.59	2.408	0.00829	0
433	500	0.115	2	50	2.44	1098	15.30	2.900	46.64	3.475	0.144	0
700	500	0.071	2	50	1.51	679	5.85	2.900	17.84	5.619	0.148	0
900	500	0.056	2	48	1.17	528	3.44	2.983	10.50	7.431	0.115	0
1200	1000	0.083	2	48	0.90	539	3.60	3.212	5.482	5.335	0.00518	0
1800	1000	0.056	2	48	0.62	373	1.72	2.983	2.624	7.431	0.00230	0
2400	1000	0.042	2	48	0.47	280	0.968	2.983	1.476	9.908	0.00173	0
3000	1000	0.033	2	49	0.35	216	0.774	2.983	0.9446	12.384	0.00276	0

from (53), which derives from (32) using the previously chosen values of d_o and V_P and assumes $N_{tot} = N_{io} + 2N_{row}$. This equation essentially insures that there are enough I/O resonators N_{io} to satisfy the termination resistance R_Q requirement. Once known, the number of columns must be such that the row-column product (which equals N_{tot}) exceeds $N_{io} + N_b$. For the current design, the number of needed I/O resonators is 15, making the combined I/O and buffer count 23. This requires at least 6 columns, making for a total of 24 resonators per quadrant.

The remaining $N_{tot} - (N_{io} + N_b) = 1$ can then serve as a tuning electrode. If the single disk resonator manufacturing resonance frequency standard deviation is known, then (55) computes the

number of tuning resonators needed to attain perfectly tuned filter fabrication yields of 68.3%, 95.4%, and 99.7% for i equal to 1, 2, and 3, respectively. The designer can merely increase the dc-bias and/or add a column if yield requirements call for more tuning resonators. For the Part II demonstrated filter, the addition of 1V to the design-flow dc-bias to make $V_P = 17\text{V}$ allows reduction of the needed I/O resonator number to 14, allowing for 2 tuning resonators while retaining 24 resonators total in a quadrant. This is still less than the 3 recommended by (56) for 68.3% perfect-tuned yield, but is sufficient for the demonstrated research prototype.

This quadrant design yields an R_Q of 445 Ω close to the desired 450 Ω . Further massaging of dc-bias and row-column

choices can get even closer to this target, if needed.

From here, the dimensions of the coupling beams come readily from the indicated expressions. These then permit assembly of the fully balanced structure of Fig. 2, which in turn yields the complete equivalent circuit of the filter for SPICE verification shown in Fig. 25. Table I in Part II includes all dimensions and geometry considerations to allow for the complete layout of a filter satisfying the stated specification.

A. Filter Design Examples

To give a sense of what types of filters might be desirable in an RF front-end bank, Table IV presents example designs for various 2nd order Chebyshev differential filters requiring $R_Q=50\Omega$ and with center frequencies ranging from 50MHz to 3GHz assuming 3 μm -thick polysilicon structural material. The columns grouped under the 'filter specifications' section of Table IV specify the filter center frequency, bandwidth, and insertion loss as design objectives. The filter design procedure summarized in Table III then yields the values listed under the 'Calculated Design Variables' section of Table IV that satisfy the corresponding filter specifications. All designs assume a fabrication process using 3- μm -thick polysilicon structural material and 20-nm electrode-to-resonator gaps. Here, three different values of dc-bias that increase with increasing center frequency help to maintain the needed (C_x/C_o) 's. In addition, each design assumes the minimum required single-resonator Q value indicated in the table.

Table IV illustrates the one-to-one relation between example RF channel-select communication standard requirements, i.e., filter spectral masks, and the geometric dimensions of the final on-silicon filter product. The fact that lateral dimensions (instead of the thickness) specify each filter constitutes a key advantage of this design approach, since it means the whole filter bank is amenable to automatic generation by a computer-aided design (CAD) program [1]. Such a program could very quickly generate the layouts required to achieve all filter responses, making realization of a VLSI circuit of such filters as convenient as already the case for transistor IC design.

Note that several of the lower frequency designs in the table use already achievable resonator performance, as evidenced by Part II of this paper and by the summary of achieved (C_x/C_o) and Q combinations in Fig. 21 of [20]. However, this table is perhaps most useful in identifying needed resonator attributes and challenges at the higher frequencies. In particular, it predicts that application of already achieved gap spacings (e.g., from [34]) to disk resonators should allow channel-select filters at the prescribed high frequencies, as long as 12V dc-biases are permissible, and as long as the indicated Q minima are attainable. The jury is still out on polysilicon Q , but CVD diamond material readily provides the needed Q [43].

It is worth noting that some of the coupling beam widths in Table IV for filters past 1.8 GHz become quite small. If too small, then one solution is to use coupling beams that are multiples of a quarter-wavelength. For example, use of $5\lambda/4$ beams instead of $\lambda/4$ takes the needed 1.8-GHz filter coupling beam width from 208nm to 1.04 μm .

Table V summarizes the Fig. 25 equivalent circuit element values for each of the Table IV filter designs. To demonstrate

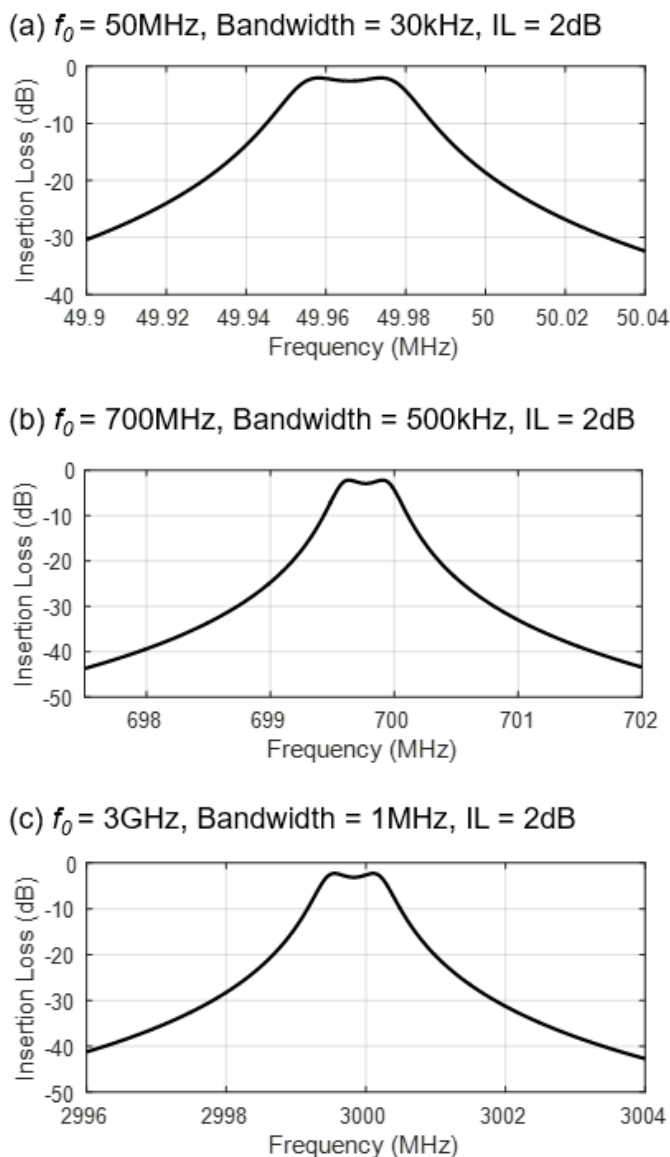


Fig. 26: SPICE simulated frequency responses for a 2nd order 50 Ω terminated 0.5dB ripple 2dB insertion loss Chebyshev filter with (a) 30kHz bandwidth at 50MHz. (b) 500kHz bandwidth at 700MHz. (c) 1MHz bandwidth at 3GHz

the utility of the equivalent circuit, Fig. 26 plots SPICE simulated frequency responses for three of the filters within the 50MHz to 3GHz frequency range, each properly terminated with 50 Ω .

As Table IV demonstrates, capacitive transduced vibrating disk filter technology can adapt to challenging channel-select filter specifications over a wide frequency range by merely adjusting numerous design knobs, such as voltage, electrode-to-resonator gap spacing, and array size. Table IV makes it clear that the combination of capacitive transducer gap scaling and array-composite scaling is key to achieving RF channel-selection at 1GHz and beyond with a small area footprint. While the need for 70 resonators in each array-composite in the 3-GHz design of the last row might seem daunting, note that the total filter quadrant area can be as small as 0.00064mm², so a 4-quadrant filter consumes 0.00256mm². Indeed, 9765 of such filters (without bond pads) could fit in a 5mm \times 5mm chip.

Still, filters at GHz frequencies will be challenging. Fortunately, there is no need to ponder feasibility at VHF, as Part II of this paper demonstrates.

XIV. CONCLUSION

This Part I of two papers introduced a design flow for micro-mechanical RF channel-select filters capable of eliminating strong adjacent channel blockers directly after the antenna, which greatly reduces power consumption in RF front-ends. Electromechanical analogies that model the resonance behavior of filter building blocks, such as vibrating disk resonators, capacitive actuation electrodes, and coupling beams, facilitate the use of conventional LC ladder filter design tables and methods as the starting point for filter design. This in turn simplifies realization of familiar filter types, e.g., Chebyshev, Butterworth, Linear Phase, etc.

While known filter design methods readily achieve ideal designs, they do not address the non-idealities of micromechanical realization, which include high single-device impedance, shunt I/O capacitance, finite coupler stiffness, stress, and fabrication process variations. The methods described herein address these issues via a combination of device scaling and mechanical circuit design. Specifically, capacitive transducer gap scaling very effectively raises electromechanical coupling (C_x/C_o) to needed values. The use of mechanically coupled resonator array-composites then permits tailoring of impedance values, resonator-to-resonator coupling, mismatch tolerances, and stress relief to outright enable design of practical filters. Finally, balanced differential design suppresses both electrical and mechanical spurious responses. These design strategies will likely become indispensable as the frequency and order of micromechanical filters increase to meet the demands of practical next-generation commercial transceivers.

Perhaps the most significant contribution of this work is its demonstration of an intuitive hierarchical mechanical circuit design flow that is technology agnostic and that empowers a designer in much the same way that intuition facilitates transistor circuit design. Part II of this paper gauges the efficacy of this design approach via fabrication and measurement of a 224-MHz 0.1% bandwidth RF channel-select filter generated via the methodology outlined herein.

XV. REFERENCES

- [1] C. T.-C. Nguyen, "MEMS-based RF channel selection for true software-defined radio and low-power sensor communications," *IEEE Commun. Mag.*, vol. 51, no. 4, pp. 110-119, 2013.
- [2] C. T.-C. Nguyen, "Frequency-selective MEMS for miniaturized low-power communication devices," *IEEE Trans. Microw. Theory Tech.*, vol. 47, no. 8, pp. 1486-1503, 1999.
- [3] J. W. Park and B. Razavi, "Channel selection at RF using Miller bandpass filters," *IEEE J. of Solid-State Circuits*, vol. 49, no. 12, pp. 3063-3078, Dec. 2014.
- [4] T. O. Rocheleau, T. L. Naing, J. N. Nilchi and C. T.-C. Nguyen, "A MEMS-based RF channel-selecting super-regenerative transceiver for wireless sensor nodes," in *Tech. Dig. Solid-State Sensors, Actuators, and Microsystems Workshop*, Hilton Head Island, SC, 2014, pp. 1-4.
- [5] European Telecommunications Standards Institute (ETSI) 3rd Generation Partnership Project (3GPP), "Technical specification group radio access network: User equipment (UE) radio transmission and reception (TDD) (3GPP TS 25.102 V13.3.0 Release 13)," 2016-01.
- [6] European Telecommunications Standards Institute (ETSI) 3rd Generation Partnership Project (3GPP), "Technical specification group radio access network: GSM/EDGE radio transmission and reception (3GPP TS 45.005 V13.3.0 Release 13)," 2016-12.
- [7] C. T.-C. Nguyen, "MEMS technology for timing and frequency control," *IEEE Trans. Ferroelectr. Freq. Control*, vol. 54, no. 2, pp. 251-270, 2007.
- [8] T.-T. Yen, C.-M. Lin, Y.-J. Lai, D. Wittwer, M. A. Hopcroft and A. P. Pisano, "Fine frequency selection techniques for aluminum nitride Lamb wave resonators," in *Proc. IEEE Int. Frequency Control Symp.*, Newport Beach, CA, 2010, pp. 9-13.
- [9] C. Zuo, N. Sinha, M. B. Pisani, C. R. Perez, R. Mahameed and G. Piazza, "Channel-select RF MEMS filters based on self-coupled AlN contour-mode piezoelectric resonators," in *Proc. IEEE Int. Ultrasonics Symp.*, New York, NY, 2007, pp. 1156-1159.
- [10] B. Kim, R. H. Olsson and K. E. Wojciechowski, "AlN microresonator-based filters with multiple bandwidths at low intermediate frequencies," *J. Microelectromech. Syst.*, vol. 22, no. 4, pp. 949-961, 2013.
- [11] R. H. Olsson, C. M. Washburn, J. E. Stevens, M. R. Tuck and C. D. Nordquist, "VHF and UHF mechanically coupled aluminum nitride MEMS filters," in *Proc. IEEE Int. Frequency Control Symp.*, Honolulu, HI, 2008, pp. 634-639.
- [12] D. Weinstein, H. Chandralim, L. F. Cheow and S. A. Bhawe, "Dielectrically transduced single-ended to differential MEMS filter," in *Tech. Dig. IEEE Int. Solid-State Circuits Conf.*, San Francisco, CA, 2006, pp. 1236-1243.
- [13] H. Chandralim, D. Weinstein, L. F. Cheow and S. A. Bhawe, "High- κ dielectrically transduced MEMS thickness shear mode resonators and tunable channel-select RF filters," *Sens. Act. A: Phys.*, vol. 136, no. 2, pp. 527-539, 2007.
- [14] K. Wang and C. T.-C. Nguyen, "High-order medium frequency micromechanical electronic filters," *J. Microelectromech. Syst.*, vol. 8, no. 4, pp. 534-557, 1999.
- [15] F. D. Bannon, J. R. Clark and C. T.-C. Nguyen, "High-Q HF microelectromechanical filters," *IEEE J. Solid-State Circuits*, vol. 35, no. 4, pp. 512-526, 2000.
- [16] S.-S. Li, Y.-W. Lin, Z. Ren and C. T.-C. Nguyen, "A micromechanical parallel-class disk-array filter," in *Proc. Joint IEEE Int. Frequency Control Symp. and European Frequency and Time Forum*, Geneva, Switzerland, 2007, pp. 1356-1361.
- [17] C.-Y. Chen, M.-H. Li, C.-H. Chin and S.-S. Li, "Implementation of a CMOS-MEMS filter through a mixed electrical and mechanical coupling scheme," *IEEE J. Microelectromech. Syst.*, vol. 25, no. 2, pp. 262-274, April 2016.
- [18] S. Pourkamali, R. Abdolvand and F. Ayazi, "A 600 kHz electrically-coupled MEMS bandpass filter," in *Proc. IEEE 16th Int. Conf. on Micro Electro Mech. Syst. (MEMS'03)*, Kyoto, Japan, Jan. 2003, pp. 702-705.
- [19] S.-S. Li, Y.-W. Lin, Z. Ren and C. T.-C. Nguyen, "An MSI micromechanical differential disk-array filter," in *Tech. Dig. Int. Conf. Solid-State Sensors, Actuators, and Microsystems (Transducers '07)*, Lyon, France, 2007, pp. 307-311.
- [20] L.-W. Hung and C. T.-C. Nguyen, "Capacitive-Piezoelectric transducers for high-Q micromechanical AlN resonators," *Journal of Microelectromechanical Systems*, vol. 24, no. 2, pp. 458-473, 2015.
- [21] R. A. Schneider and C. T.-C. Nguyen, "On/off switchable high-Q capacitive-piezoelectric AlN resonators," in *Tech. Digest, 2014 IEEE Microelectromech. Syst. Conf.*, San Francisco, California, January 26-30, 2014, pp. 1265-1268.
- [22] M. Akgul and C. T.-C. Nguyen, "A passband-corrected high rejection channel-select micromechanical disk filter," in *Frequency Control Symposium (FCS), the 2014 IEEE Int.*, May 2014.
- [23] J. Wang, Z. Ren and C. T.-C. Nguyen, "1.156-GHz self-aligned vibrating micromechanical disk resonator," *IEEE Trans. Ultrason. Ferroelectr. Freq. Control*, vol. 51, no. 12, pp. 1607-1628, 2004.
- [24] M. Akgul, B. Kim, Z. Ren and C. T.-C. Nguyen, "Capacitively transduced micromechanical resonators with simultaneous low motional resistance and $Q > 70,000$," in *Tech. Dig. Solid-State Sensors, Actuators,*

and *Microsystems Workshop*, Hilton Head Island, SC, 2010, pp. 467-470.

- [25] M. U. Demirci and C. T.-C. Nguyen, "Mechanically corner-coupled square microresonator array for reduced series motional resistance," *J. Microelectromech. Syst.*, vol. 15, no. 6, pp. 1419-1436, 2006.
- [26] H. Nathanson, W. E. Newell, R. A. Wickstrom and J. R. Davis Jr., "The resonant gate transistor," *IEEE Trans. Electron Devices*, vol. 14, no. 3, pp. 117-133, 1967.
- [27] M. Akgul, Z. Ren and C. T.-C. Nguyen, "Voltage-controlled tuning to optimize MEMS resonator array-composite output power," in *Proc. Joint IEEE Int. Frequency Control Symp. and European Frequency and Time Forum*, San Francisco, CA, 2011, pp. 1-6.
- [28] M. Akgul, "A Micromechanical RF Channelizer," in *Ph.D. Dissertation*, Dept. of Electrical Engineering and Computer Sciences, University of California, Berkeley, CA, 2014.
- [29] A. I. Zverev, *Handbook of filter synthesis*, New York: Wiley, 1967.
- [30] A. S. Sedra and P. O. Brackett, *Filter Theory and Design: Active and Passive*, Beaverton, OR: Matrix, 1978.
- [31] L. Wu, M. Akgul, Z. Ren, Y. Lin, W.-C. Li and C. T.-C. Nguyen, "Hollow stems for higher micromechanical disk resonator quality factor," in *Proc. IEEE Ultrasonics Symp.*, Orlando, FL, 2011, pp. 1964-1967.
- [32] J. Wang, J. E. Butler, T. Feygelson, and C. T.-C. Nguyen, "1.51-GHz nanocrystalline diamond micromechanical disk resonator with material mismatched isolating support," in *Proceedings, the 17th IEEE Int. Conf. on Micro Electro Mechanical Systems (MEMS)*, Maastricht, The Netherlands, Jan. 25-29, 2004, pp. 821-824.
- [33] M. Akgul, L. Wu, Z. Ren and C. T.-C. Nguyen, "A negative capacitance equivalent circuit model for parallel-plate capacitive-gap transduced micromechanical resonators," *IEEE Transactions on Ultrasonic, Ferroelectrics, and Frequency Control*, vol. 61, no. 5, pp. 849-869, May 2014.
- [34] J. N. Nilchi, R. Liu and C. T.-C. Nguyen, "High Cx/Co 13nm-capacitive-gap transduced disk resonator," in *Tech. Dig. 30th IEEE Int. Conf. on Micro Electro Mechanical Systems (MEMS)*, Las Vegas, NV, 2017, pp. 924-927.
- [35] Y.-W. Lin, S.-S. Li, Z. Ren and C. T.-C. Nguyen, "Low phase noise array-composite micromechanical wine-glass disk oscillator," in *Tech. Dig. IEEE Int. Electron Devices Mtg.*, Washington, DC, 2005, pp. 287-290.
- [36] A. Erbes, P. Thiruvengathan, J. Woodhouse and A. A. Seshia, "Numerical study of the impact of vibration localization on the motional resistance of weakly coupled MEMS resonators," *IEEE J. of Microelectromechanical Syst.*, vol. 24, no. 4, pp. 997-1005, Aug. 2015.
- [37] A. Bloch, "Electromechanical analogies and their use for the analysis of mechanical and electromechanical systems," *Electr. Eng. - Part Gen. J. Inst. Of*, vol. 92, no. 52, pp. 157-169, 1945.
- [38] R. Johnson, *Mechanical filters in electronics*, Wiley, 1983.
- [39] Y.-W. Lin, S.-S. Li, Z. Ren and C. T.-C. Nguyen, "Third-order intermodulation distortion in capacitively-driven VHF micromechanical resonators," in *Proc. IEEE Int. Ultrasonics Symp.*, Rotterdam, Netherlands, 2005, pp.1592-1595.
- [40] A. T. Alastalo and V. Kaajakari, "Third-order intermodulation in microelectromechanical filters coupled with capacitive transducers," *J. of Microelectromech. Syst.*, vol. 15, no. 1, pp. 141-148, Feb. 2006.
- [41] D. Pozar, *Microwave Engineering*, Wiley, 1997.
- [42] P. W. Tuinenga, *SPICE: A Guide to Circuit Simulation and Analysis Using PSpice*, NJ: Prentice Hall, 1995.
- [43] T. L. Naing, T. O. Rocheleau, Z. Ren, S.-S. Li and C. T.-C. Nguyen, "High-Q UHF spoke-supported ring resonators," *IEEE J. of Microelectromechanical Syst.*, vol. 25, no. 1, pp. 11-29, Feb. 2016.
- [44] L.-W. Hung and C. T.-C. Nguyen, "Capacitive-piezoelectric AIN resonators with $Q > 12,000$," in *Tech. Dig. 24th IEEE Int. Conf. on Micro Electro Mechanical Systems (MEMS)*, Cancun, Mexico, 2011, pp. 173-176.



Alper Ozgurluk (S'12) received the B.S. degree in Electrical and Electronics Engineering from Bilkent University, Ankara, Turkey. He is currently working towards his Ph.D. degree in Electrical Engineering and Computer Sciences at the University of California at Berkeley.

His research interests include capacitive-gap transduced large-scale integrated (LSI) micromechanical circuits, high- Q wide-tunable ruthenium metal resonators, and integrated CMOS-MEMS systems.



Mehmet Akgul (S'07) received the Ph.D. in Electrical Engineering and Computer Sciences at the University of California at Berkeley in 2014. He received the B.S. degree in Electrical and Electronics Engineering from the Middle East Technical University, Ankara, Turkey, as second in his class in 2007.

His PhD research focused on the design, microfabrication, and testing of medium-scale integrated micromechanical circuits using capacitive-gap transduced resonators as building blocks, with a primary focus on RF filters for ultra-low power radio applications. He also studied diamond materials for high- Q mechanical resonators and explored the use of ALD high- k dielectrics to strengthen electromechanical coupling by partially filling electrode-to-resonator gaps towards the sub-40 nm range.

In 2014, he joined TDK InvenSense as a Sr. MEMS Design Engineer, where he worked as a MEMS inertial measurement unit (IMU) designer with a specific focus on optical image stabilization (OIS) gyroscopes. In 2015, he joined Google, where he is presently a Sr. Hardware Design Engineer. His current focus is on sensor fusion algorithms for better location and context user experience in mobile platforms.



Clark T.-C. Nguyen (S'90-M'95-SM'01-F'07) received the B. S., M. S., and Ph.D. degrees from the University of California at Berkeley in 1989, 1991, and 1994, respectively, all in Electrical Engineering and Computer Sciences.

In 1995, he joined the faculty of the University of Michigan, Ann Arbor, where he was a Professor in the Department of Electrical Engineering and Computer Science up until mid-2006.

In 2006, he joined the Department of Electrical Engineering and Computer Sciences at the University of California at Berkeley, where he is presently the Conexant Systems Distinguished Professor and a Co-Director of the Berkeley Sensor & Actuator Center. His research interests focus upon micro electromechanical systems (MEMS) and include integrated micromechanical signal processors and sensors, merged circuit/micromechanical technologies, optomechanical devices, RF communication architectures, and integrated circuit design and technology. In

2001, Prof. Nguyen founded Discera, Inc., a company aimed at commercializing communication products based upon MEMS technology, with an initial focus on the very vibrating micro-mechanical resonators pioneered by his research in past years. He served as Vice President and Chief Technology Officer (CTO) of Discera until mid-2002, at which point he joined the Defense Advanced Research Projects Agency (DARPA) on an IPA, where he served for four years as the Program Manager of ten different MEMS-centric programs in the Microsystems Technology Office of DARPA.

Prof. Nguyen won the IEEE Cady Award in 2006, the IEEE Robert Bosch Micro and Nano Electro Mechanical Systems Award in 2017, and together with his students has garnered more than twelve best paper awards from IEEE conferences and journals focused on frequency control and MEMS. From 2007 to 2009, he served as a Distinguished Lecturer for the IEEE Solid-State Circuits Society. Prof. Nguyen was the Technical Program Chair of the 2010 IEEE Int. Frequency Control Symposium and a Co-General Chair of the 2011 Combined IEEE Int. Frequency Control Symposium and European Frequency and Time Forum, as well as a Co-General Chair of the 2017 IEEE Int. Micro Electro Mechanical Systems Conference. From 2008 to 2013, he served as Vice President of Frequency Control in the IEEE Ultrasonics, Ferroelectrics, and Frequency Control Society, after which he became the society President from 2016 to 2017. He is currently the Junior Past-President of the society.